CHALMERS
UNIVERSITY OF TECHNOLOGY

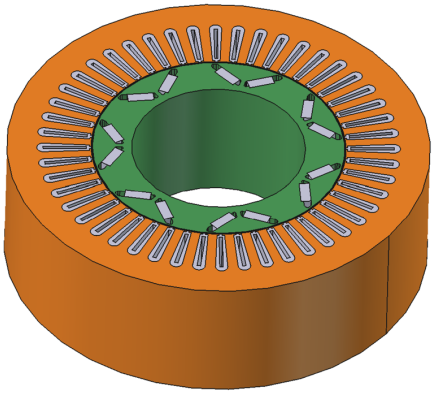

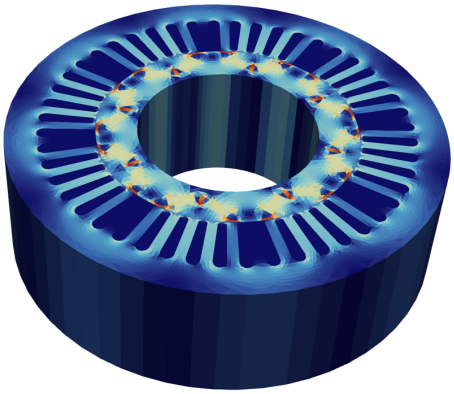

# Electric Machine 3D FEM Modeling and Design Impact on Torque Ripple

EENX30 - Master's thesis in mobility engineering

Jiyang Fan
Xiance Wu

Department of Mechanics and Marinetime Sciences
CHALMERS UNIVERSITY OF TECHNOLOGY
Gothenburg, Sweden 2026
www.chalmers.se

Master's thesis 2026

# Electric Machine 3D FEM Modeling and Design Impact on Torque Ripple

Jiyang Fan
Xiance Wu


CHALMERS
UNIVERSITY OF TECHNOLOGY

Department of Mechanics and Maritime Sciences
Chalmers University of Technology
Gothenburg, Sweden 2026

Electric Machine 3D FEM Modeling and Design Impact on Torque Ripple



Supervisor: Dr. Raik Orbay (Technical Expert)
Department of Strategy and Program Execution, Volvo Cars Corporation

Co-Supervisor: Dr. Joachim Härsjö (Technical Leader)
Department of Strategy and Program Execution, Volvo Cars Corporation

Co-Supervisor: Johan Cederlund (Technical Expert)
Department of Electric Driveline, Volvo Cars Corporation

Examiner: Professor Torbjörn Thiringer
Department of Electrical Engineering, Chalmers University of Technology

Master's Thesis 2026
Department of Mechanics and Maritime Sciences
Chalmers University of Technology
SE-412 96 Gothenburg
Telephone +46 31 772 1000

Cover:

Typeset in LaTeX
Printed by Chalmers Reproservice
Gothenburg, Sweden 2026

# Abstract

A Gmsh mesh model of the Prius 2004 IPMSM was established using Gmsh built-in programming language; all geometrical entities, mesh properties, and boundary conditions were defined programmatically in scripts. Depending on the pole-slot combination, a slice model can be conveniently generated by specifying the number of circumferential sections as a constant parameter in the scripts.

Furthermore, no-skew and two types of skewed rotor configurations of Prius IPMSM 2004 were simulated in Ansys Maxwell. The results showed that both torque ripple and cogging torque were reduced under skewed configurations. Compared with the no-skew rotor, the torque ripple reduced from 30.6% to 12.2% in the herringbone (known as V-shape) and 11.9% in the linear skew design; in terms of cogging torque, it was reduced from 1.1 N.m to 0.8 N.m in the herringbone and 0.6 N.m in the linear skew. Cross-validation between Ansys Maxwell 2D and ElmerFEM 2D demonstrates that back-EMF and flux linkage are in good agreement, confirming the reliability of the Elmer setup for the simulation of Prius motor.

Finally, the ElmerFEM 3D results showed good agreement with the 2D results in terms of back-EMF harmonic content. In particular, the $11^{\text{th}}$ and $13^{\text{th}}$ harmonics were significantly reduced with a skewing angle of 3.75°, while the fundamental magnitude remained nearly unchanged.



Keywords: ElmerFEM, 3D-FEM, skew, torque ripple, cogging torque, back-EMF, harmonic.

# Acknowledgements

This thesis was carried out at Volvo Car Corporation (VCC) in the Department of Strategy and Program Execution. We are grateful for the opportunity given by VCC to work in a real engineering environment, where we are able to connect the knowledge acquired during academic studies to the real-world engineering. The access to both software and hardware, along with the professional working environment, enabled us to bridge the gap between theory and industrial application.

We would like to express our sincere gratitude to our supervisor, Dr. Raik Orbay, for his continuous and unconditional support throughout our thesis work. His guidance in theory, modeling, and simulation tools has been invaluable, enabling us to develop a more structured and comprehensive understanding of real-world engineering problems. His insightful feedback has been essential in keeping our work on the right track. Moreover, his dedication and sense of humor have greatly motivated us to persevere through challenges and pressure during the project.

We are also grateful to our co-supervisors, Johan Cederlund and Joachim Härsjö, for their support and guidance. Their extensive experience in various areas of automotive engineering helped us navigate the project more efficiently and in the right direction. In addition, the valuable materials they provided gave us deeper insight into real-world automotive engineering practice.

We would also like to express our gratitude to our examiner, Professor Torbjörn Thiringer from Chalmers University of Technology, for his valuable input regarding our research direction. His feedback helped us clarify several key issues in the project. Moreover, his useful advice and early-stage guidance enabled us to conduct the thesis in a more structured manner. This project represents an important milestone in our transition from academic studies to professional engineering practice, and the experience gained will be valuable for our future careers.

Last but not least, we would like to thank our colleagues in the department for their continuous support and assistance throughout the project. In particular, we would like to express our sincere appreciation to Anders Bergqvist, Joachim Lindström, and Johannes Emilsson. Whether in technical discussions or daily work, their willingness to share knowledge and provide guidance has greatly contributed to our learning experience and fostered a strong sense of team spirit.

Jiyang Fan, Gothenburg, 2026
Xiance Wu, Gothenburg, 2026

# List of Acronyms

Below is the list of acronyms that have been used throughout this thesis listed in alphabetical order:

| | |
|---|---|
| 2D | Two-Dimensional |
| 3D | Three-Dimensional |
| AC | Alternating Current |
| Back-EMF | Back Electromotive Force |
| BiCGStab | Biconjugate Gradient Stabilized |
| CAD | Computer-Aided Design |
| EMF | Electromotive Force |
| EV | Electric Vehicle |
| FFT | Fast Fourier Transform |
| GCR | Generalized Conjugate Residual |
| LSM | Loss Separation Method |
| ICE | Internal Combustion Engine |
| IDRM | Induced Dimension Reduction Method |
| ILU | Incomplete LU-decomposition |
| IM | Induction Motor |
| IPMSM | Interior Permanent Magnet Synchronous Machine |
| MMF | Magnetomotive Force |
| NTF | Normalized Torque Fluctuation |
| NVH | Noise, Vibration and Harshness |
| P2P | Peak-to-Peak |
| PDE | Partial Differential Equation |
| PMSM | Permanent Magnet Synchronous Motor |
| RMF | Rotating Magnetic Field |

# Contents

# 1
# Preface

Volvo Car Corporation (VCC), founded in Gothenburg in 1927, has been reputable for safety, reliability, and Scandinavian engineering values. Throughout its history, the company has continuously introduced technologies aimed at improving vehicle safety, driving experience, and overall mobility. From pioneering safety innovations in earlier decades to today's transition towards electrification and intelligent vehicles, Volvo Cars continues to evolve together with the changing demands of society and transportation.

VCC is one of the OEMs that started developing electric vehicles early; its first pure electric model-C30 Electric was delivered to market in 2011. In 2015, Volvo Cars introduced its global electrification strategy, which aimed to integrate plug-in hybrid electric vehicles (PHEVs) across the entire product portfolio, develop battery electric vehicles (BEVs), and establish electrification-oriented platform architectures such as SPA and CMA. The company's initial objective was to become a fully electric vehicle brand by 2030.

Compared with ICE vehicles, EVs are much more environmentally friendly, more efficient, quieter, and smoother thanks to the unique advantages of electric propulsion systems. However, EVs also present new challenges related to driving smoothness, vibration, and acoustic performance, as these effects are more perceptible in the absence of engine noise. Torque ripple is one of the perspectives that can be optimized to improve customer satisfaction. Figure 1.1 shows the latest VOLVO EX60 (800V) equipped with a skewed rotor topology in its electric motor [2].

**Figure 1.1:** Volvo EX60

# 2

# Introduction

## 2.1 Background

Permanent magnet synchronous machines (PMSMs) have become one of the most widely used machine types in modern electric vehicle (EV) propulsion systems due to their high efficiency, compact structure and high power density [3]. Compared with conventional induction machines (IMs), PMSMs are able to provide better efficiency and torque performance under low-speed and partial-load operating conditions, which make them suitable for automotive traction applications.

Despite these advantages, PMSMs are also associated with several electromagnetic phenomena, including torque ripple and harmonic distortion. These effects are mainly related to the interaction between stator slotting, permanent magnets, and harmonic components in the air-gap magnetic field. Excessive torque ripple may lead to additional vibration and acoustic noise, which can influence the NVH (Noise, Vibration and Harshness) performance and driving comfort of electric vehicles. Therefore, reducing torque ripple while maintaining the electromagnetic performance of the machine has been an important and everlasting topic in PMSM analysis and design.

Several methods have been proposed to reduce torque ripple, including rotor skewing, optimized slot-pole combinations, and harmonic current injection [4]. Among these approaches, rotor skewing is commonly used because it can effectively reduce cogging torque without significantly affecting the average torque output. However, skewing also introduces additional spatial electromagnetic effects along the axial direction, which are difficult to fully represent using simplified 2D models.

To investigate these electromagnetic behaviors, finite element method (FEM) analysis is widely used in both industrial development and academic research. While 2D FEM models are computationally efficient and suitable for preliminary investigations, full 3D FEM models can provide additional information regarding axial magnetic-field distribution and spatial electromagnetic behavior under skewed rotor configurations. In recent years, open-source FEM platforms such as ElmerFEM have also attracted increasing attention due to their flexibility for customized electromagnetic modeling and high-performance computing applications.

## 2.2 Literature study

To model a PMSM, the electromagnetic behavior of the motor is of great importance for the assessment of the motor's performance, which is mainly governed by Maxwell equations. Magnetic flux distribution, magnetic flux path, and torque production can be explained by the classic electromagnetic field theory. In a PMSM, the rotor provides a constant magnetic field by the permanent magnets inside, while the stator generates a rotating magnetic field when supplied with alternating current (AC). The interaction of these two fields produces torque on the shaft [5]. Hendershot et al. [6] systematically introduced the fundamental theory and common modeling assumptions of electric motors and explained the relationships among flux linkage, electromagnetic torque, and motor geometry. This theoretical framework gives us a firm physical basis for our analysis and serves as the foundation for later simulation methods.

With the development of simulation tools and modeling approaches, 2D FEM modeling of PMSM has become more mature. Ponomarev [7] formed a complete workflow using Gmsh and ElmerFEM, including geometry construction, material definition, boundary conditions, and post-processing of key performance indices. This tutorial provides a practical and reproducible implementation of 2D FEM for PMSM analysis.

Various research studies are being carried out to compare 2D and 3D FEM models of PMSM. Naik et al. built both 2D and 3D models of an IPMSM and compared the results of flux linkages, back electromotive force (back-EMF), electromagnetic torque, and losses. The results were overall accurate and trustworthy. However, there was a noticeable difference between the two models since the axial magnetic field effect was assumed to be zero [8]. Similarly, Pechlivanidou et al. presented that 3D FEM can capture end effects and spatial flux distribution more accurately, while the computational cost is relatively higher [9]. Based on the flexibility in changing the design given by 3D modeling, some studies focus on the influence of different skew strategies. By keeping the overall structure unchanged and only tuning the skew angle, Xiaodong et al. investigated the skew effect on the back-EMF waveforms and harmonic components. This study showed that skew reduces the vibration of the back-EMF waveform and the amplitude of cogging torque [10]. Tsunata & Takemoto's study systematically classified common skew arrangements, including continuous and step skew. The results indicate that a properly designed skew structure can reduce cogging torque and back-EMF harmonics and subsequently electromagnetic excitation forces, which lead to improved noise, vibration, and harshness (NVH) performance.

Although 3D FEM simulation shows more detailed electromagnetic effects, its high computational cost limits its use in multi-case comparisons. Sasaki and Igarashi proposed a deep learning-based approach to accelerate electromagnetic topology optimization. By training surrogate models using FEM simulation data, the number of required FEM evaluations can be significantly reduced without losing accuracy [11]. These studies indicate that data-driven methods pave the way for exploring

complex 3D design and modeling in the future and offer convenience and flexibility in case optimization

## 2.3 Objective

The purpose of this work is to establish a 2D model using the built-in scripting language of Gmsh as the foundation for electromagnetic analysis and subsequent 3D finite element analysis (FEA) in ElmerFEM. Furthermore, another objective is to investigate flux linkage, back-EMF, and harmonic characteristics through 2D electromagnetic analysis, and to compare the obtained results with those from ANSYS Maxwell in order to validate the consistency and feasibility of the developed model and analysis procedure. In addition, a target is to analyze and quantify the effects of several skewing configurations on torque ripple, cogging torque, and losses. Finally, a goal is to explore the application of 3D FEM analysis for investigating flux linkage, back-EMF, harmonic characteristics, and the influence of skewing on back-EMF harmonics.

## 2.4 Limitations

There are several limitations in this study. Firstly, the analysis focuses highly on electromagnetic performance, while thermal and mechanical effects are not considered. Secondly, boundary conditions are used to represent the surrounding world to limit the size of the model and reduce computing time; for example, input voltage and cooling effects are not considered. Additionally, the accuracy of the results depends on mesh quality and computational resources, which may limit the level of geometric detail. Finally, the study considers a limited set of skew arrangements due to the fact that the main purpose of this study is to discover the law of skew, and the findings may not be able to generalize all possible designs.

# 3
# Theory

## 3.1 Electromagnetic Fundamentals

Throughout the thesis work, Maxwell's equations [14] play an essential role as the theoretical basis since they describe the fundamental behavior of electromagnetic fields. The equations provide a mathematical model for electric motors, and how the electromagnetic fields are generated by charges, currents, and changes in the fields is well defined by them.

### 3.1.1 Gauss's Law

Gauss's law [15] describes the relationship between electric charge and electric field as

$$\nabla \cdot \mathbf{E} = \frac{\rho}{\varepsilon_0} \tag{3.1}$$

In this expression, $\nabla \cdot \mathbf{E}$ describes the divergence of the electric field, $\varepsilon_0$ is the permittivity of vacuum space, and $\rho$ represents the charge density distributed within a unit volume.

Gauss's law for magnetic flux density [16] is given by

$$\nabla \cdot \mathbf{B} = 0 \tag{3.2}$$

This equation states that there is no divergence in the magnetic field, meaning that the magnetic field lines are inherently continuous and form closed loops all the time. Here, $\nabla \cdot \mathbf{B}$ is the divergence of the magnetic flux density $\mathbf{B}$.

### 3.1.2 Faraday's Law

Faraday's law of electromagnetic induction [17] is expressed as

$$\nabla \times \mathbf{E} = -\frac{\partial \mathbf{B}}{\partial t} \tag{3.3}$$

This equation describes a time-varying magnetic field inducing an electric field and $\partial \mathbf{B}/\partial t$ denotes the time derivative of the magnetic flux density. In electrical machines, the rotating magnetic field produces a time-varying magnetic flux, which induces a voltage in the stator windings, and the back electromotive force (back-EMF) is generated.

### 3.1.3 Ampère–Maxwell Law

The Ampère-Maxwell [18] law is given by

$$\nabla \times \mathbf{B} = \mu_0 \left( \mathbf{J} + \varepsilon_0 \frac{\partial \mathbf{E}}{\partial t} \right), \tag{3.4}$$

which indicates that magnetic fields arise from both conduction currents and time-varying electric fields. In this expression, $\nabla \times \mathbf{B}$ represents the curl of the magnetic flux density, $\mu_0$ denotes the permeability of free space, $\mathbf{J}$ is the current density, and the term $\varepsilon_0 \frac{\partial \mathbf{E}}{\partial t}$ is the displacement current associated with a time-varying electric field. In electrical machines, the magnetic fields generated by stator currents interact with the rotor magnetic field, resulting in the production of electromagnetic torque.

## 3.2 PMSM Fundamental

In general, the working principle of a PMSM depends on the interaction between the rotating magnetic field generated by the stator windings and the magnetic field produced by the permanent magnets mounted on the rotor. For a three-phase PMSM, the windings are spatially distributed at 120-degree intervals and are supplied with three-phase AC currents.

### 3.2.1 Three-phase AC system

Since the three-phase currents are phase-shifted by 120°, their combined effect produces a rotating magnetic field inside the electrical machine. This rotating behavior can be represented not only by sinusoidal waveforms in the time domain but also by space vectors in the spatial domain. Figure 3.1 illustrates both representations of a balanced three-phase current system. The upper plot shows the sinusoidal variation of phase currents $i_a$, $i_b$, and $i_c$ with respect to time, while the lower plot presents the corresponding current space vectors in the $\alpha$-$\beta$ reference frame [19]. The three vectors are separated by 120° electrically and together form the basis of space vector analysis used in AC machine modeling and control.

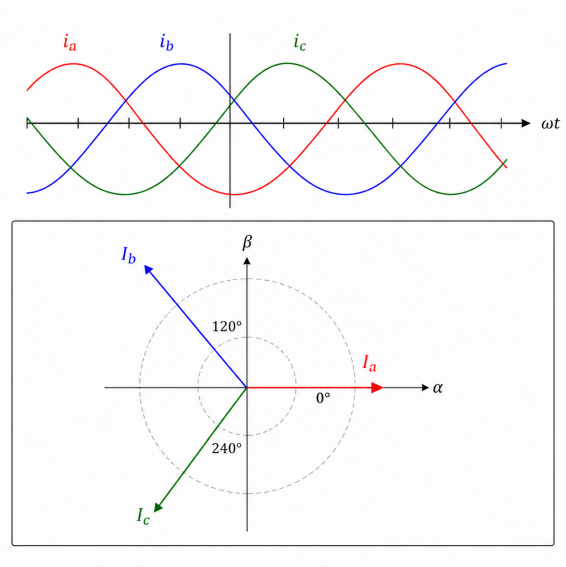


**Figure 3.1:** Space vectors

### 3.2.2 d-q System

In order to investigate the flux and torque in a straightforward way, 3-phase electric entities [19] need to be simplified to benefit from mathematical expression and electric drive control. Assume there is no zero-sequence in phases A, B, and C; they can be expressed by

$$i_a(t) = I_m \cos(\omega t) \tag{3.5}$$
$$i_b(t) = I_m \cos(\omega t - 120°) \tag{3.6}$$
$$i_c(t) = I_m \cos(\omega t + 120°) \tag{3.7}$$

where $I_m$ is the amplitude (maximum value) of the phase current and $\omega$ is the angular frequency of the AC signal.

First, the Clarke transformation [20] is used to transform the three-phase currents from the *abc* frame into the stationary $\alpha$-$\beta$ frame

$$\begin{bmatrix} i_\alpha \\ i_\beta \end{bmatrix} = \frac{2}{3} \begin{bmatrix} 1 & -\frac{1}{2} & -\frac{1}{2} \\ 0 & \frac{\sqrt{3}}{2} & -\frac{\sqrt{3}}{2} \end{bmatrix} \begin{bmatrix} i_a \\ i_b \\ i_c \end{bmatrix} \tag{3.8}$$

Through this transformation, the three-phase current system can be expressed as a two-dimensional current space vector in the stationary reference frame. This helps describe the rotating magnetic field generated by the stator currents.

The Park transformation [21] is then applied to transform the stationary $\alpha$-$\beta$ components into the rotating *d*-*q* reference frame

$$\begin{bmatrix} i_d \\ i_q \end{bmatrix} = \begin{bmatrix} \cos\theta_e & \sin\theta_e \\ -\sin\theta_e & \cos\theta_e \end{bmatrix} \begin{bmatrix} i_\alpha \\ i_\beta \end{bmatrix} \tag{3.9}$$

where $\theta_e$ is the electrical rotor position.

In the *d-q* reference frame, the AC quantities can be represented as nearly constant values under steady-state operation. This makes the analysis of PMSM flux, torque, and current control more straightforward.

### 3.2.3 Rotor configurations of PMSMs

Based on the rotor configuration, PMSMs can be categorized into surface-mounted PMSMs (SPMSMs) and interior PMSMs (IPMSMs). In SPMSMs, the permanent magnets are mounted on the surface of the rotor. In this configuration, the magnetic flux paths along the d-axis and q-axis are similar. Therefore, the magnetic reluctance in both directions is assumed to be nearly the same, and the inductance in the d-axis and q-axis are approximately equal ($L_d \approx L_q$).

In contrast, permanent magnets are mounted inside the rotor in the PMSM. This configuration means that the flux paths along the d-axis and q-axis are different. The d-axis flux passes through the magnets, which have low permeability, while the q-axis flux mainly flows through iron, which has high permeability. As a result, the magnetic reluctance differs between the two directions, leading to different values of inductance ($L_d < L_q$). Because of this difference, not only the interaction between stator current and magnet flux generates torque, but also the reluctance effect. The comparison of both types of PMSMs is presented in Figure 3.2 used by UNICO [22].

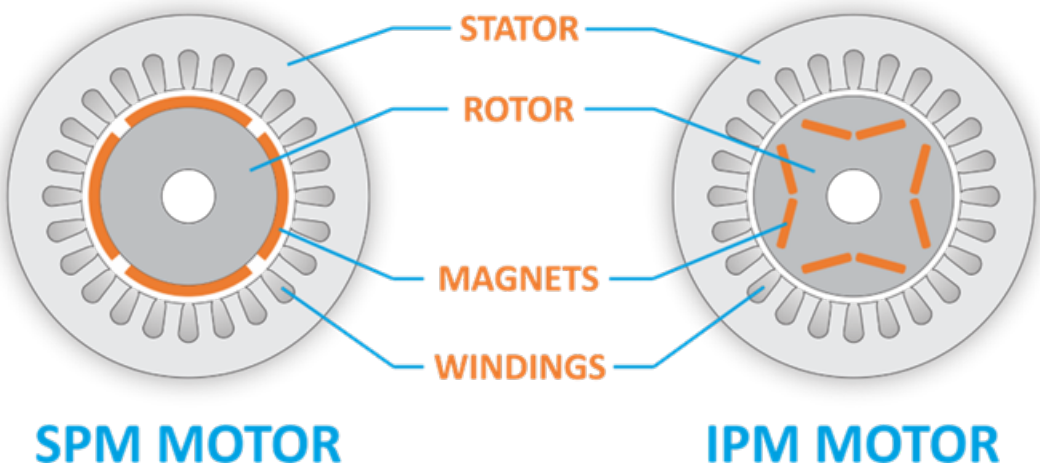


**Figure 3.2:** Comparison of rotor structures in SPMSM and IPMSM

The Toyota Prius electric motor is a representative example of an IPMSM. The rotor design of the Prius allows efficient utilization of magnetic materials while maintaining strong electromagnetic performance. Due to the complex magnetic field distribution and rotor geometry, detailed analysis of such machines typically relies on numerical methods such as finite element analysis.

## 3.3 Electromagnetic Quantities in PMSMs

### 3.3.1 Flux linkage

Flux linkage [23] is a fundamental electromagnetic quantity that describes the coupling between the stator windings and the magnetic field in a permanent magnet synchronous machine (PMSM). For a winding with $N$ turns, the flux linkage is defined as

$$\lambda = N\Phi, \tag{3.10}$$

where $\Phi$ is the magnetic flux linked with a single turn. The magnetic flux [23] through a surface $S$ bounded by the conductor is

$$\Phi = \int_S \mathbf{B} \cdot d\mathbf{S}. \tag{3.11}$$

The magnetic vector potential formulation, and the magnetic flux density is expressed as

$$\mathbf{B} = \nabla \times \mathbf{A}. \tag{3.12}$$

The magnetic flux then is expressed as

$$\Phi = \int_S (\nabla \times \mathbf{A}) \cdot d\mathbf{S}. \tag{3.13}$$

Then the Stokes' theorem [24] converts the surface integral into a line integral along the boundary of the turn, and it gives

$$\Phi = \oint_{\partial S} \mathbf{A} \cdot d\mathbf{l}. \tag{3.14}$$

Although the line-integral expression is compact and useful for theoretical derivations, practical finite-element models of electrical machines typically describe the stator windings as distributed conductor regions inside the slots. In such cases, the flux linkage can be obtained more conveniently by integrating the axial component of the magnetic vector potential, $A_z$, over the conductor area, and it is expressed as

$$\Phi = \frac{1}{S} \int_S A_z \, dS, \tag{3.15}$$

where $S$ is the cross-sectional area filled by the winding conductors.

For a real stator phase winding, the conductors are divided into two groups: the in-going conductors representing the positive direction, located in area $S_+$, and the out-going conductors that carry current in the negative direction, located in area $S_-$. Since these directions are opposite, their flux contributions must be subtracted. Including the effective axial stack length $l$, the total flux linkage of the phase winding becomes

$$\lambda = Nl \left( \frac{1}{S_+} \int_{S_+} A_z \, dS - \frac{1}{S_-} \int_{S_-} A_z \, dS \right), \tag{3.16}$$

where l stands for the stack length. In finite-element-based electromagnetic solvers, the equation above employing magnetic vector potential formulations is usually used, especially in distributed windings and 2D/3D fields where there are complex slot geometries.

### 3.3.2 Back electromotive force

The back electromotive force (back-EMF) in a PMSM is derived from the fundamental law that a change in the magnetic environment produces an electromotive force in the stator winding. According to Faraday's law, the magnitude of this voltage is directly proportional to the rate of change of flux linkages. On the other hand, Lenz's law determines the sign of this voltage so that it opposes changes in flux linkages. This gives us the expression for back-EMF [25] in a PMSM

$$e(t) = -\frac{d}{dt}\lambda(t), \tag{3.17}$$

### 3.3.3 Harmonic content in back-EMF

The waveform of back-EMF is one of the most important indicators of PMSM performance. Based on the theory mentioned above, the flux linkage is presented as a sinusoidal waveform. The back-EMF is obtained by taking time derivative of flux linkage. As a result, it should ideally exhibit a sinusoidal waveform.

However, in a real-world PMSM, as the magnetic field passes through the slot openings, the distortions are produced in the air-gap flux density, which cause the irregularities and unsmoothness in the phase flux linkage. While this minor variation in flux linkage can result in amplified fluctuations in the waveform of back-EMF.

Even though the waveform is dominated by the first-order fundamental component, there are noticeable spikes in the back-EMF waveform, which can be treated as high-order harmonic components. This motivates further study in harmonic characteristics.

To describe the harmonic components observed in the back-EMF waveform, a Fourier-series-based representation [26] is adopted. Accordingly, the back-EMF can be expressed as

$$e(t) = a_0 + \sum_{n=1}^{\infty} \left[a_n \cos(n\omega t) + b_n \sin(n\omega t)\right], \tag{3.18}$$

where

- $n$ is the harmonic order,
- $\omega$ is the fundamental electrical angular frequency,
- $a_0$ is the DC component,
- $a_n$ and $b_n$ are the Fourier coefficients of the $n$-th harmonic.

For case comparison, it is necessary to quantify the overall distortion level of the waveform. Using total harmonic distortion (THD) [27] is common for this purpose, providing us with a compact measure of all harmonic components relative to the first-order wave. The THD is defined as

$$\mathrm{THD} = \frac{\sqrt{\sum_{n=2}^{N} E_n^2}}{E_1}. \tag{3.19}$$

A higher THD normally means that there is more significant waveform distortion, which can lead to increased torque ripple, acoustic noise, or additional losses.

## 3.4 Torque

### 3.4.1 Cogging torque

Cogging torque [28], also known as detent or no-current torque, is generated from the interaction between the rotor permanent magnets and the stator slot openings. It is caused by the periodic variation of the magnetic field when the magnets pass the stator teeth. As the rotor rotates, the magnetic field distribution changes periodically, which produces torque even without stator current excitation.

### 3.4.2 Electromagnetic torque

When fed with current, torque is produced by the interaction between the stator magnetic field and the magnetic field of the rotor permanent magnets. In simple terms, the stator current creates a rotating magnetic field, and this field pulls the rotor, resulting in electromagnetic torque.

In the *d*-*q* reference frame, the electromagnetic torque [29] of an IPMSM can be expressed as

$$T_e = \frac{3}{2} p \left[ \psi_f i_q + (L_d - L_q) i_d i_q \right], \tag{3.20}$$

where $p$ is the number of pole pairs, $\psi_f$ is the permanent magnet flux linkage, $i_d$ and $i_q$ are the currents in the *d*- and *q*-axes respectively, and $L_d$ and $L_q$ are the corresponding inductances.

As shown in the torque equation, the torque has two main parts: one comes from the permanent magnets, and the other comes from the difference between $L_d$ and $L_q$. In IPMSM, this difference creates an additional torque component, which improves the overall torque capability.

## 3.5 Core Loss

When assessing magnetic properties and the performance of the PMSM, core loss is one of the key indicators, which is produced under the effect of alternating magnetic fields by the magnetic materials. It is commonly divided into three parts: hysteresis loss, eddy-current loss, and excess loss (or anomalous loss) [30]. The overall loss can be expressed as the sum of the three losses

$$P_c = P_h + P_e + P_{ex}. \tag{3.21}$$

### 3.5.1 Hysteresis loss

Hysteresis loss is the dissipation of energy in the form of heat. It is produced in ferromagnetic materials due to the irreversible process of magnetization. It exists

during every magnetization-demagnetization cycle even though the input current waveform is perfectly sinusoidal. In Bertotti's extended model of the loss separation method (LSM) [30], the hysteresis loss is expressed as

$$P_h = k_h f B_s^x, \tag{3.22}$$

where $k_h$ is the empirical hysteresis coefficient, $f$ is the frequency, $B_s$ is the magnetic flux density, and $x$ is an empirical exponent.

### 3.5.2 Eddy loss

According to Faraday's law, an eddy current is induced within conductors either by a changing magnetic field in the conductor or by a relative motion between a conductor and the magnetic field. This current generates Joule heat as energy dissipation due to the resistivity of the material [31]. In the LSM, it is given as

$$P_e = k_e f^2 B_s^2, \tag{3.23}$$

For laminated materials, a more detailed form can be written as

$$P_e = \frac{\pi^2 d^2 f^2 B_s^2}{\rho} \beta, \tag{3.24}$$

where $k_e$ is the empirical eddy-current loss coefficient, $d$ is the thickness of lamination, $\rho$ is the electrical resistivity, and $\beta$ is the magnetic induction exponent [30].

### 3.5.3 Excess loss

Other than hysteresis loss and eddy-current loss, there are some other kinds of losses that are not clearly defined. In this case, excess loss is used to fill this blank. In the LSM, this term is added to improve the accuracy of the total loss estimation
In Bertotti's model [30], the excess loss is expressed as

$$P_{ex} = k_{ex} f^{1.5} B_s^{1.5}, \tag{3.25}$$

where $k_{ex}$ is the empirical excess loss coefficient.

## 3.6 ElmerFEM

ElmerFEM [32] is a powerful open-source simulation software, which supports parallel computation and offers convenience in using a number of solvers for better accuracy. ElmerFEM mainly focuses on FEM and includes multiple physical models such as fluid dynamics, structural mechanics, electromagnetics, heat transfer, and acoustics.

In finite element analysis, the partial differential equations (PDEs) are discretized and linearized. After these steps, the original computation can be transformed into a system of linear algebraic equations in the form of

$$Ax = b, \tag{3.26}$$

where $A$ is the coefficient matrix derived from the discretization, $b$ is the right-hand side vector that represents external sources, which are of orders $n \times n$ and $n \times 1$, respectively. And $x$ is the matrix of unknowns.

### 3.6.1 Iteration method

Generally, the iteration method in ElmerFEM can be categorized into Direct Method and Iterative Method.

Direct Method aims to compute the solution in a finite number of operations without any initial reference. Umfpack and Mumps are two of the most widely used direct methods in 2D modeling. As a result, the output is highly robust and more trustworthy. However, its limitations are also notable. First, the computational load is extremely heavy. Then, the memory requirement is large. Lastly, as a result, for some large-scale cases, such as 3D simulation, this method has limited applicability [34].

In contrast, iterative methods compute the solution by continuously improving an initial guess through iterations. Starting from an initial approximation $x^{(0)}$, the solution is updated in the form

$$x^{(k+1)} = x^{(k)} + \text{correction}, \tag{3.27}$$

where the correction term is used to refine the current estimation. The residual [33] is defined as

$$r^{(k)} = b - Ax^{(k)}, \tag{3.28}$$

which measures the error of the current approximation. The objective of iterative methods is to reduce the norm of the residual during the iteration process and finally obtain a relatively accurate result.

Most iterative solvers in Elmer are using the Krylov subspace methods[34]. These methods construct a sequence of subspaces generated by the initial residual and seek approximate solutions within these subspaces. The Krylov subspace of dimension $k$ is defined as [35]

$$\mathcal{K}_k(A, r_0) = \text{span}\{r_0, Ar_0, A^2r_0, \ldots, A^{k-1}r_0\}, \tag{3.29}$$

where $r_0 = b - Ax^{(0)}$ is the initial residual. By projecting the original system onto these subspaces, Krylov methods are able to efficiently approximate the solution with relatively low computational effort.

Biconjugate Gradient Stabilized (BiCGStab), Generalized Conjugate Residual (GCR), and Induced Dimension Reduction Method (IDR(s)) are commonly used in Elmer for 3D cases. The BiCGStab method is expected to offer smoother convergence for non-symmetric linear systems. The GCR method can improve the solutions at each iteration, though at the cost of higher computational burden and memory requirements. In comparison, the IDR(s) method makes convergence more efficient by reducing the dimension of the residual space, achieving better performance with relatively lower memory consumption and smooth convergence behavior [34].

### 3.6.2 Preconditioning strategy

As shown in Equation 3.26, the finite element discretization gives a linear system of the form $Ax = b$. In the computations of FEM, the iterative solvers are usually combined with some preconditioning strategies to improve the efficiency of convergence.

The preconditioning technique is typically applied to transform the original system into an equivalent form that is easier to converge. In ElmerSolver, this is achieved by solving [34]

$$AM^{-1}z = b, \tag{3.30}$$

where $M$ means a preconditioner that approximates the matrix $A$, and the relation between the variables is given by $z = Mx$. In practice, the $M^{-1}$ is normally not needed; instead, the preconditioning step only involves solving linear systems of the form [34]

$$Mu = v. \tag{3.31}$$

Incomplete LU-decomposition (ILU) is one of the most widely used strategies since it allows us to find a good balance between convergence performance and computational cost. The method constructs an approximate LU factorization of the coefficient matrix $A$ by removing fill-in elements generated during the factorization process optionally [34]. The ILU preconditioner is combined with Krylov methods such as GCR, meaning that the linear system can be solved efficiently without consuming a large amount of memory.

## 3.7 FEM Meshing

In an FEM-based simulation, the method to handle interfaces between mesh regions is of great importance and has crucial impact on the accuracy and stability of the solution especially when different meshes are used for different physical domains. Elmer provides us a number of mesh treating strategies to fulfill different simulation requirements. Discontinuous boundary, conforming mesh and mortar boundary are three of the most widely used methods that correspond to different levels of meshing complexity [34]. The following sections briefly introduce these three boundary treatments

### 3.7.1 Discontinuous boundary

Poor physical contact may lead to an internal jump at the interfaces. Discontinuous boundary is used to allow the discontinuities of the solution between interfaces. In this method, nodes on the interface are copied, making the degrees of freedom on both sides independent, which is suitable for modeling poorly coupled or physically separated domains [34].

In a PMSM, this treatment is particularly useful at the air gap between the stator and the rotor. If the interface was modeled as one single continuous curve, the spinning rotor would cause the stator mesh to distort, leading to the inaccuracy of

the numerical solution. By introducing the discontinuous boundary, as shown in Figure 3.3, the stator mesh and the rotor mesh are decoupled, which allows relative rotation without distortion.

**Figure 3.3:** Discontinuous boundary

### 3.7.2 Conforming mesh

Conforming Mesh is applied when the solution across an interface needs to be continuous. In this method, the meshes on both sides of the interface must be perfectly matched, and the nodes are shared as shown in Figure 3.4. Unlike the function of the Discontinuous Boundary, the solution is automatically enforced since both sides share the same degree of freedom [34]. This mesh treatment provides computational efficiency without adding constraint equations. However, it requires strict conformity between meshes and is therefore mainly applicable to cases with regular geometry and negligible relative motion.

**Figure 3.4:** Conforming mesh

### 3.7.3 Sliding mesh

Sliding Mesh is used to glue the master side and the slave side that do not match across an interface while enforcing continuity in a weak form, as shown in Figure 3.5. The treatment Mortar Boundary [34] allows information can be projected across the interface without having conforming meshes, meaning that flexibility of modeling can be ensured. As a result, Mortar Boundary is suitable for multiphysics coupling

and interfaces with relative motion, such as skewing between two segments of a PMSM rotor, where there is a particular angle apart.

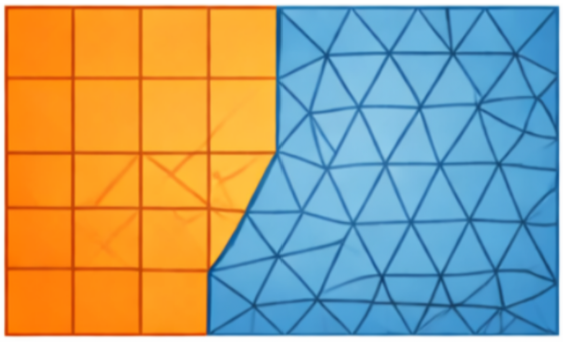

**Figure 3.5:** Mortar boundary

To wrap up, ElmerFEM offers several treatments to accommodate different mesh layouts. These treatments differ in their assumptions on mesh compatibility or solution continuity. Table 3.1 demonstrates a concise comparison of the three treatments that have been discussed above.

**Table 3.1:** Comparison of interface treatment methods in Elmer

| **Feature** | **Discontinuous boundary** | **Conforming boundary** | **Mortar boundary** |
|---|---|---|---|
| Mesh compatibility | No | Yes (exact match) | No |
| Solution continuity | Discontinuous by default | Strong continuity | Weak continuity |
| Implementation level | Mesh-level (node duplication) | Shared degrees of freedom | Constraint-based coupling |
| Additional unknowns | No | No | Yes (e.g. Lagrange multipliers) |
| Numerical complexity | Moderate | Lowest | Higher |
| Typical applications | Single interface curve with physical jumps | Matching subdomains | Non-matching mesh coupling |

# 4

# Methods

## 4.1 2D Toyota Prius 2004 Model Set-up

Due to high torque density, wide constant-power operating range, high efficiency, and excellent flux-weakening capability, V-shape IPMSMs have become one of the most widely adopted traction motor technologies in the automotive industry. In addition, their robust rotor structure, high power density, and ability to produce both magnetic and reluctance torque make them highly suitable for electric and hybrid vehicle applications requiring compact size and superior dynamic performance.

Among the various IPMSM designs, the 2004 Toyota Prius IPMSM is considered a benchmark machine because of its innovative rotor configuration, efficient electromagnetic design, and proven industrial success in hybrid electric vehicles. Therefore, it was selected as the baseline machine for investigation and analysis in this thesis.

### 4.1.1 Software workflow

In this section, the basic function of tools will be explained in detail, and the generic process flow will be presented at the end of this section.

Gmsh [36] is an open-source finite element mesh generator with a built-in CAD engine and post-processor. Its design goal is to provide a fast, lightweight, and user-friendly meshing tool with parametric input and flexible visualization capabilities. Gmsh is built around four modules (geometry, mesh, solver, and post-processing), which can be controlled with the graphical user interface; from the command line; using text files written in Gmsh's own scripting language (.geo files); or through the C++, C, Python, Julia, and Fortran application programming interfaces.

ParaView [37] is an open-source, multi-platform application designed for scientific data analysis and 3D visualization, capable of processing extremely large datasets on systems ranging from laptops to supercomputers. It allows users to interactively analyze, visualize, and extract insights from simulation data using parallel computing.

As Figure 4.1 shows, the generic process of Elmer simulation in this study is illustrated.

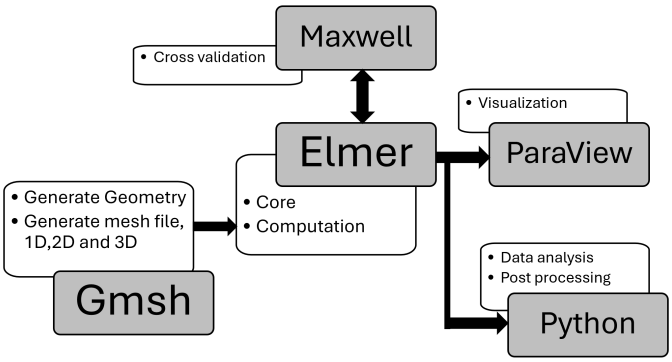


**Figure 4.1:** Process

### 4.1.2 Analytic data

The parameters listed in Table 4.1 are obtained from the ANSYS Prius 2004 model [12] and are used as the reference for the simulations in this work.

**Table 4.1:** Main data (Toyota Prius 2004)

| Item | Value |
|---|---|
| Number of slots ($Qs$) | 48 |
| Number of poles ($p * 2$) | 8 |
| Number of slots/pole/phase ($q$) | 2 |
| Shaft power ($P$) | 50000 W |
| Efficiency | 0.94–0.96 |
| Rated torque ($T_r$) | 400 N·m |
| Rated speed ($n$) | 1200–1500 rpm |
| Line-to-line voltage ($U$) | 500 V |
| Stator phase voltage ($U_{ph}$) | 288 V |
| PM-induced voltage ($E_{PM}$) | 250–300 V |
| Frequency ($f$) | 80–100 Hz |
| Stator current ($I_s$) | 200–250 A |
| Stator d-current ($I_d$) | -50 to -100 A |
| Stator q-current ($I_q$) | 180–230 A |
| Phase resistance ($R_{ph}$) | 0.02–0.05 Ω |
| Number of phase turns ($N$) | ∼30–40 |
| Wire current density ($J_s$) | 4–8 × $10^6$ A/m$^2$ |
| Windings wire diameter ($D_{Cu}$) | ∼2–4 mm |
| Number of slot conductors ($z_{Qs}$) | ∼60–80 |
| Air gap flux density peak ($B_g$) | 0.9–1.0 T |
| Stator yoke flux density ($B_s$) | 1.4–1.6 T |
| Rotor yoke flux density ($B_r$) | 1.5–1.7 T |
| Load angle | 20–35 degrees |

### 4.1.3 Geometrical and mesh set-up

There are many approaches and meshing tools available to build geometrical models for FEA computation, such as creating a 3D model in a CAD tool and exporting it as a STEP file to generate a computable mesh, or using built-in meshing tools with script-driven workflows.

With the purpose of finding an efficient way to build mesh files that fit ElmerFEM simulations, three approaches were explored. As shown in Figure 4.2, the first approach is particularly beneficial since all geometrical entities, mesh sizes, bodies, and boundary conditions are developed by Gmsh's built-in programming language in scripts. This significantly reduces the time when modifications and iterations are needed during the simulations.

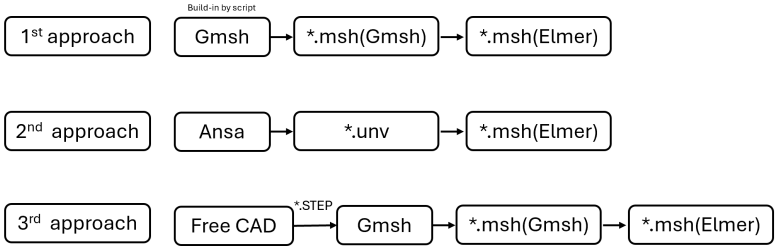


**Figure 4.2:** Modeling approach

Figure 4.3 shows the modeling process in Gmsh. The full model is built from points, lines, surfaces, to volumes. All entities are editable in the scripts, and any parameters can be modified to fit the simulation. Thanks to the parameterization of Gmsh scripts, slicing models can be easily obtained by specifying the required part of the model in Gmsh, thereby reducing the computation time depending on the constants defined in the scripts. In general, coarse mesh sizes are assigned to the outer diameter of the stator and the inner diameter of the rotor, while refined mesh sizes are assigned close to air gap areas.

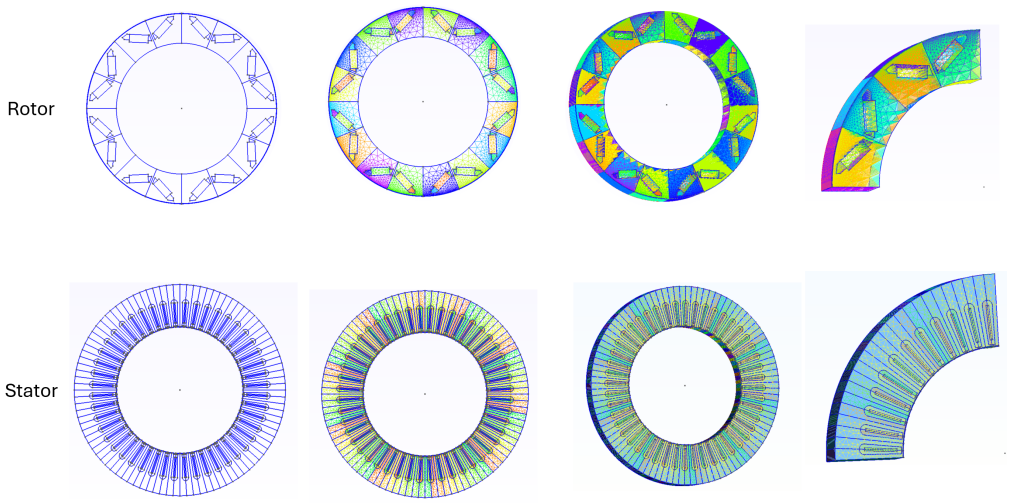


**Figure 4.3:** Prius mesh model

### 4.1.4 Material selection

In this study, in order to model the electromagnetic behavior of the PMSM, some magnetic properties are characterized using a set of key physical parameters. Air, copper windings, and magnetic materials are described by their fundamental electromagnetic properties, including density, relative permeability, electrical conductivity, and relative permittivity.

### 4.1.5 Material parameters

The parameters used for the material in this study are given in Table 4.2. The values have been chosen from engineering texts and material data books to maintain consistency within the electromagnetic simulation. These parameter values are chosen based on information found in conventional engineering handbooks and material databases, thus ensuring physical consistency of the magnetic fields simulated.

In particular, the material properties of air, copper, and permanent magnets were determined according to typical values found in the literature and databases such as material libraries from COMSOL [39], handbook data [40], and publicly available databases such as EngineeringToolbox [41]. The values of the chosen materials are listed in Table 4.2.

**Table 4.2:** Material properties

| Material | Density $\rho$ (kg/m$^3$) | $\mu_r$ | $\sigma$ (S/m) | $\varepsilon_r$ |
|---|---|---|---|---|
| Air | 1.225 | 1.0 | $\sim 0$ | $\approx 1.0006$ |
| Copper | 8960 | 1.0 | $5.8 \times 10^7$ | $\approx 1$ |
| Magnet | 7500 | 1.1 | $\sim 6 \times 10^5$ | $\approx 1$ |

### 4.1.6 Nonlinear steel lamination

In addition to the linear materials mentioned above, the laminated steel used in the stator and rotor core is modeled as a nonlinear magnetic material. Unlike air, copper, and permanent magnets, its magnetic characteristics cannot be accurately represented by a constant relative permeability. Therefore, the nonlinear magnetic behavior is described using a B-H lookup table [12].

As shown in Figure 4.4, the B-H curve represents the relationship between the magnetic flux density $B$ and the magnetic field intensity $H$. It can be observed that the material exhibits nonlinear saturation behavior: the magnetic flux density increases rapidly at low field intensity, while a much larger increase in $H$ is required as the material approaches saturation.

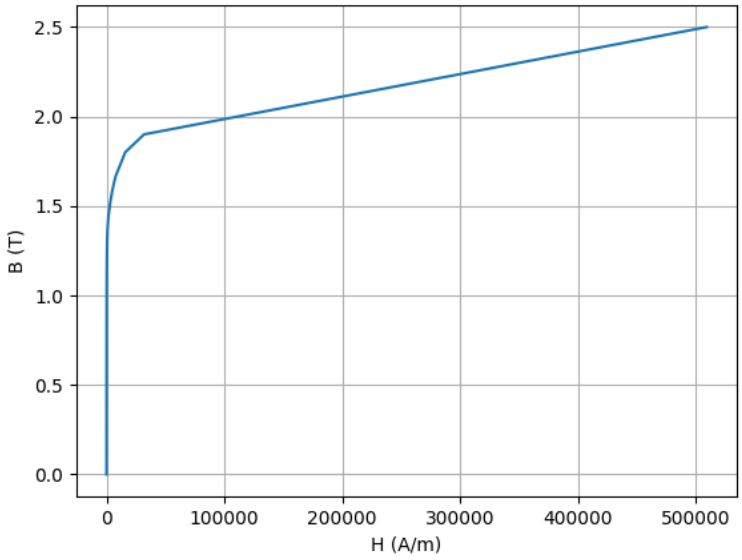


**Figure 4.4:** The B-H curve of M19 29G

### 4.1.7 Solver introduction

In this study, key parameters are calculated by the solvers in ElmerFEM. The most important solver is MagnetoDynamics [42].

#### 4.1.7.1 MagnetoDynamics2D

In the two-dimensional electromagnetic simulation, the MagnetoDynamics2D solver is used to calculate the magnetic field distribution in the cross-section of the motor. This solver is designed for 2D magnetic cases, where the main unknown is the $A_z$, which is the magnetic vector potential along the z-direction.

In the computation of 2D PMSM, the current density is normally perpendicular to the analyzed plane. Thus, the scalar electric potential is not necessarily accounted

for as an unknown in the A-V formulation. As a result, only the magnetic potential in the z-direction can describe the electromagnetic problems. Based on the $A_z$, the magnetic flux density, magnetic field distribution, and some other electromagnetic quantities can be obtained.

MagnetoDynamics2D can also support both time-domain and frequency-domain simulations. The time-domain formulation is mainly applied when observing the variation of rotor position and the electromagnetic torque over time or the mechanical rotor rotation angle. The frequency-domain analysis can be used to study harmonics and estimate the Joule losses in both the stator and rotor. The calculated magnetic vector potential is further post-processed to obtain other quantities, among which flux linkage and back-emf are very important to observe.

#### 4.1.7.2 WhitneyAV

In the three-dimensional electromagnetic simulation, the WhitneyAV solver [42] is applied for the calculation. The solver, similarly, is based on A-V formulation. However, in 3D cases, the current distribution is no longer limited to single direction. Therefore, unlike the 2D solver, the scalar electric potential $V$ must be taken into account to accurately represent the current flow and electric field in conductive regions.

The numerical model uses edge elements to discretize the magnetic vector potential, whereas the scalar potential is discretized by nodal elements. Tangential continuity of the electromagnetic field on the boundary of elements is maintained in this approach, and a non-physical solution to the problem is avoided.

#### 4.1.7.3 FourierLossSolver

Once the solution for the electromagnetic field has been obtained, then the Fourier loss solver will take charge of estimating the iron loss based on the Steinmetz approach [43].

The time-varying magnetic flux density can be expressed in the form of harmonics component as

$$\mathbf{B}(x,t) \approx \mathbf{B}_0(x) + \sum_{k=1}^{K} \mathbf{B}_k(x) \cos\left[k\omega(t-t_0) - \phi_k\right], \tag{4.1}$$

where $k$ represents the harmonic order and $\mathbf{B}_k$ is the amplitude of the $k$-th harmonic component. The frequency of the $k$-th harmonic is defined as

$$f_k = \frac{k\omega}{2\pi}. \tag{4.2}$$

For each harmonic component, the corresponding iron loss is estimated using a Steinmetz-type equation [42], which gives

$$P_k = \int_\Omega C f_k^\alpha B_k^\beta \, d\Omega, \tag{4.3}$$

where $C$, $\alpha$, and $\beta$ are material-dependent empirical loss coefficients.

According to this solver, the total iron loss is then obtained by summing the contributions from all harmonic components.

#### 4.1.7.4 Solver parameters

The key solver parameters used in these solvers described above are listed in Table 4.3, while the remaining settings are kept default. Most commonly used iteration methods, including BiCGStab, GCR, and IDR(s), show different characteristics in terms of convergence behavior, computational efficiency, and memory usage.

**Table 4.3:** Configured parameters in ElmerFEM solvers

| **Parameter** | **MagnetoDynamics solver** | **FourierLoss solver** |
|---|---|---|
| Procedure | WhitneyAVSolver | FourierLossSolver |
| Target variable | AV | AV |
| Iterative method | IDR(s) | BiCGStab(l) |
| Preconditioning | ILU1 | ILU0 |
| Linear convergence tolerance | $1.0 \times 10^{-7}$ | $1.0 \times 10^{-3}$ |
| Maximum linear iterations | 5000 | 4500 |

The choice of preconditioning is based on the behavior of convergence. When slow convergence or divergence occurs, preconditioners (e.g., ILU) are employed to improve the stability. Similarly, the value of the convergence tolerance is defined to improve the numerical accuracy. However, the trade-off between accuracy and computational cost should be considered and requires a massive amount of tests to achieve. Last but not least, these parameters need further adjustment if the model configuration or computational environment changes.

## 4.2 3D Toyota Prius 2004 Model Set-up

### 4.2.1 Extrusion

The 2D model was directly extruded into 3D geometry with the stack length of 84 mm, as shown in Figure 4.5. The 3D was obtained by granting an axial value to all 2D geometries.

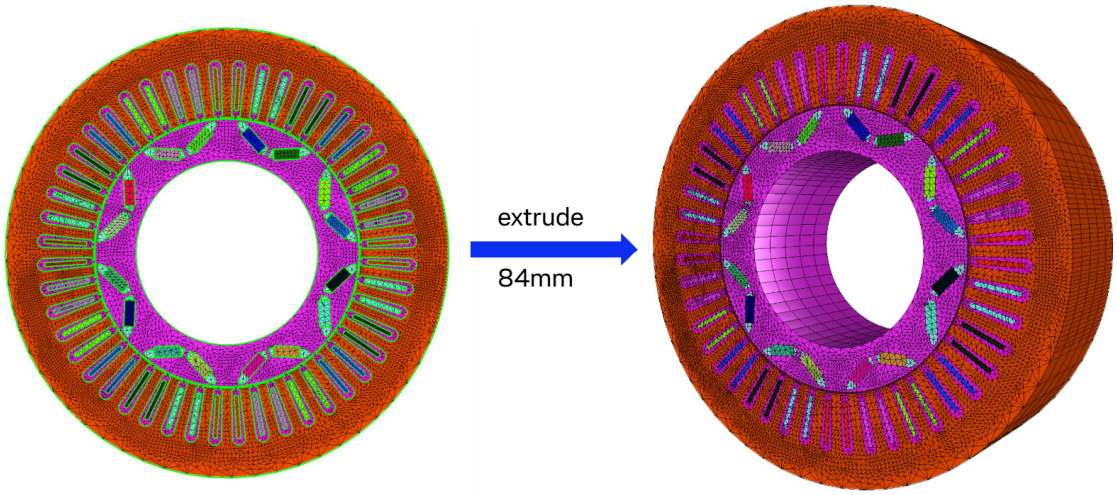


**Figure 4.5:** Extrusion from 2D to 3D

In a multi-slice 2D model, continuous axial geometry can hardly be captured since the machine was approximated by several stacked 2D slices. By contrast, direct extrusion maintains geometric continuity and therefore gives more realistic representation. However, the fully extruded model may have difficulties with convergence during computation.

Table 4.4 summarizes the main extrusion parameters in the 3D model generation, including the axial extrusion range, the number of mesh layers, and the layer spacing settings applied during the extrusion process.

**Table 4.4:** Extrusion parameters for the 3D model

| **Parameter** | **Value** | **Description** |
|---|---|---|
| Extruded Divisions | 1 | Single extrusion region |
| Extruded Limits | 0–84 mm | Axial extrusion length |
| Extruded Ratios | 1.0 | Uniform layer spacing |
| Extruded Elements | 5 | Number of mesh layers along axial direction |

### 4.2.2 Model constraints and excitations

To describe the 3D FEM model properly, a set of boundary conditions and external excitation is applied.

#### 4.2.2.1 Dirichlet boundary

The magnetic field is formulated using the magnetic vector potential. A Dirichlet boundary condition is imposed on the external boundaries including the outer, shaft, top, and bottom surfaces, where the magnetic vector potential is set to be 0 (see all surfaces in green in Figure 4.6). As a result, magnetic flux is prevented from leaving the computational domain, avoiding non-physical flux leakage caused by truncation and ensuring a proper close loop for flux and numerical stability.

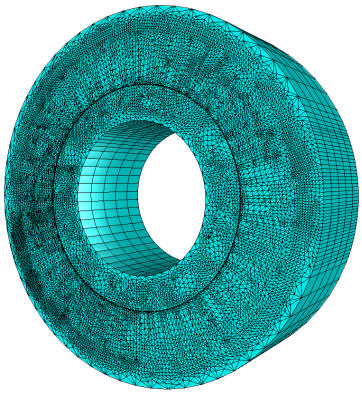

**Figure 4.6:** Dirichlet boundary condition (A=0)

#### 4.2.2.2 Mortar boundary

In the air-gap area between the rotor and the stator, a sliding mesh method is applied to handle the relative rotational motion and the unmatched meshes on both sides of the surface. Mortar method is applied to enforce the continuity of the magnetic vector potential in a weak sense, which allows non-conforming meshes to be coupled without node-to-node correspondence. In addition, it should be noted that this method is also applicable to fix the misplacement of permanent magnets in a skewed motor. The coupling is formulated within the Galerkin framework [44]. In the Galerkin framework, the governing equation is expressed in a weak form, where the solution satisfies a weighted integral equation given by

$$a(u, v) = f(v), \tag{4.4}$$

which allows the continuity condition at the interface to be enforced in an integral sense, enabling the coupling of non-conforming meshes.

#### 4.2.2.3 External excitation

The external excitations are described in the form of body force in the simulation and consist of two main parts: the mechanical rotation of the rotor and the current excitation in the stator windings. The rotational motion of the rotor is described as

$$\theta(t) = \omega_m t \tag{4.5}$$

where $\omega_m$ is the mechanical angular velocity and $t$ is time.

The three-phase currents are obtained from the inverse $dq$-to-$abc$ transformation, which gives

$$\begin{aligned} i_A &= \sqrt{2}\left(I_d \cos(\omega_e t) - I_q \sin(\omega_e t)\right), \\ i_B &= \sqrt{2}\left(I_d \cos(\omega_e t - \frac{2\pi}{3}) - I_q \sin(\omega_e t - \frac{2\pi}{3})\right), \\ i_C &= \sqrt{2}\left(I_d \cos(\omega_e t + \frac{2\pi}{3}) - I_q \sin(\omega_e t + \frac{2\pi}{3})\right). \end{aligned} \tag{4.6}$$

The current density is calculated as

$$J_{ph} = \frac{N_{ph}}{S_{cs}} i_{ph} \tag{4.7}$$

where $I_d$ and $I_q$ are the $d$-axis and $q$-axis currents, $\omega_e$ is the electrical angular frequency, $t$ is time, $N_{ph}$ is the number of turns per phase, and $S_{cs}$ is the conductor cross-sectional area.

For each phase, the positive and negative coil sides are assigned with opposite signs of current density. For instance, $A$ and $-A$ have the same magnitude but opposite directions, forming a closed current loop.

### 4.2.3 Skewing strategies in 3D

As mentioned in previous section, the rotor rotational motion is defined in external excitation. The skew structures can be generated by directly changing the mechanically rotational angle in the form of body force applied in rotor.

For example, in a two-segment skew configuration, an offset of 3.75° is applied to the rotor region where $z < 42$ mm at the first simulation time step. After saving the mesh entities, the 3.75° skewed motor is generated as illustrated in Figure 4.7

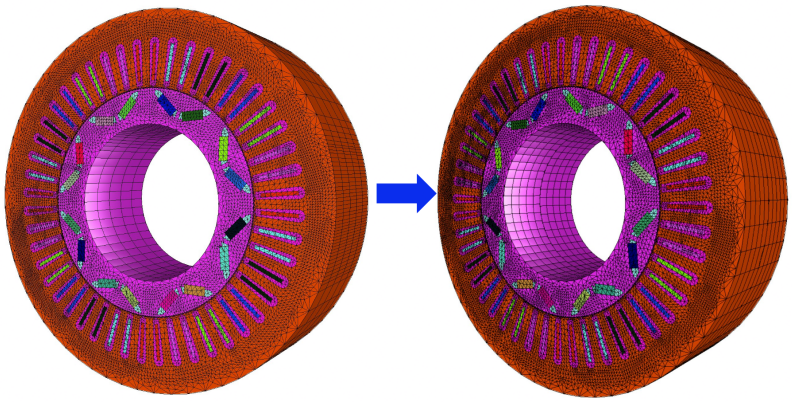

**Figure 4.7:** Generation of the two-segment skewed PMSM

Similarly, different skew angles and different segment numbers can also be generated systematically within the existing framework. This provides considerable flexibility for constructing and evaluating various skew strategies in PMSMs.

However, it should also be noted that increasing the number of skew segments will consequently introduce more geometrical discontinuities and local mesh complexity, meaning that better mesh quality and higher mesh density are needed to maintain numerical stability and simulation accuracy for more complicated skew topologies.

### 4.2.4 Parallelization

The computational cost was increased significantly because of the fully extruded 3D model. Parallel computation was therefore used to improve simulation efficiency. Parallel mesh partitioning [45] was performed using ElmerGrid, where the entire mesh model was divided into 256 parts by using the METIS partitioning method for 256 processors to run the computation of each partition simultaneously.

```
ElmerGrid 2 2 mesh -partdual -metis 256 4 -connect 1 2
```

The `-connect 1 2` option was used to keep the two air-gap Mortar boundaries within the same partition, where 1 represents the stator air gap and 2 stands for the rotor air gap. This is necessary for the correct treatment of the mortar boundary interaction at the sliding interfaces, because the coupled mortar boundaries must be handled within a common partition to ensure accuracy and consistency during computation. The resulting mesh partitioning is shown in Figure 4.8, where different colors indicate different mesh partitions used for parallel computation.

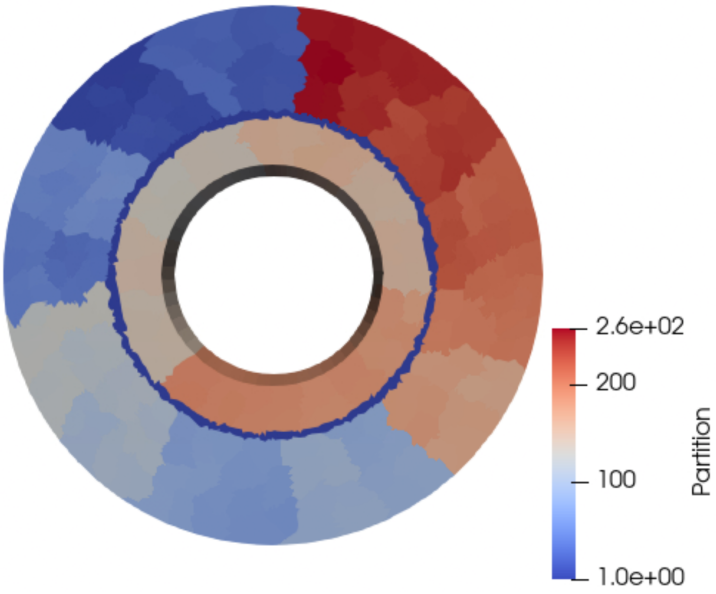


**Figure 4.8:** Mesh partitioning of the 3D model for parallel computation

# 5
# Results

## 5.1 2D electromagnetic characteristics

Prius 2004 IPMSM model is reproduced in this section as a baseline to validate the electromagnetic characteristics.

### 5.1.1 Flux linkages and back-EMF

Figure 5.1 shows the basic electromagnetic characteristics of the electric motor under a no-load cycle. Plot (a) shows the waveform of flux linkages in three phases, which exhibits a nearly perfect sinusoidal wave with a peak value of about 130 mWb. In the back-EMF waveform, there are small but noticeable spikes and local distortions at some specific rotor positions. These high-frequency behaviors appear while the rotor is passing through the stator slot openings, where the changing magnetic permeability leads to changes in magnetic field. These features reflect the effects of slot openings on the air-gap magnetic field and voltage induction.

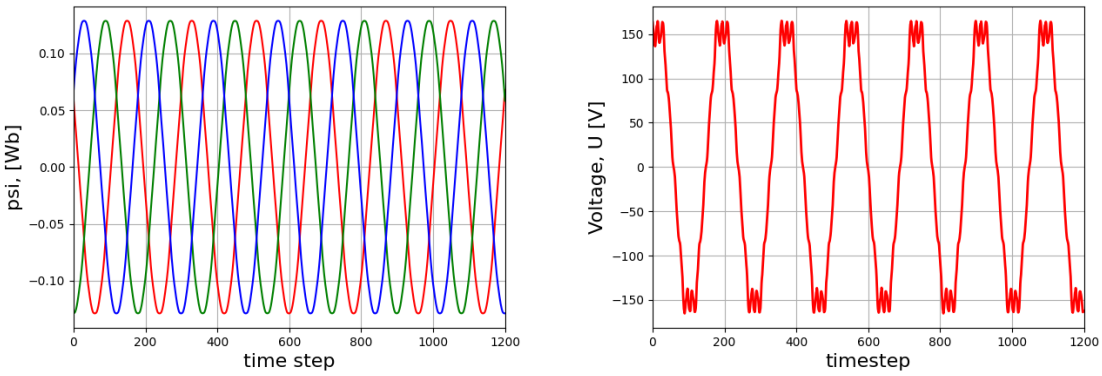


(a) (b)

**Figure 5.1:** (a) 2D Prius flux linkage. (b) 2D Prius Back-EMF.

### 5.1.2 Back-EMF harmonic

The harmonic content of back-EMF is presented in Figure 5.2. In addition to the dominant fundamental component, the $5^{\text{th}}$ and $7^{\text{th}}$ orders represent the main high-order components. The $11^{\text{th}}$ and $13^{\text{th}}$ component also exhibit a noticeable magnitude. The degree of waveform distortion can be quantified by calculating the THD,

and the value of THD is 9.15 %. This indicates that the reproduced 2D PMSM model is capable of capturing the main harmonic characteristics caused by slotting effects, providing a suitable baseline for subsequent skewing and 3D investigations.

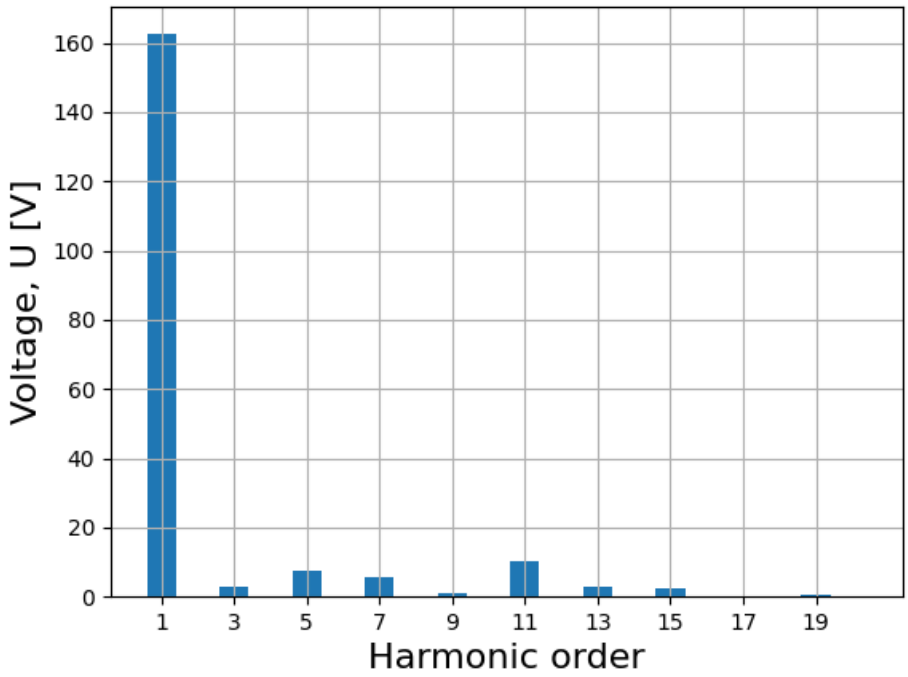


**Figure 5.2:** Harmonic content of back-EMF in 2D Prius PMSM

### 5.1.3 Dual-tool cross-validation

To further verify the consistency and reliability of the obtained electromagnetic results, an additional comparison is carried out between ElmerFEM and ANSYS Maxwell [46] using the same 2D Prius PMSM model.

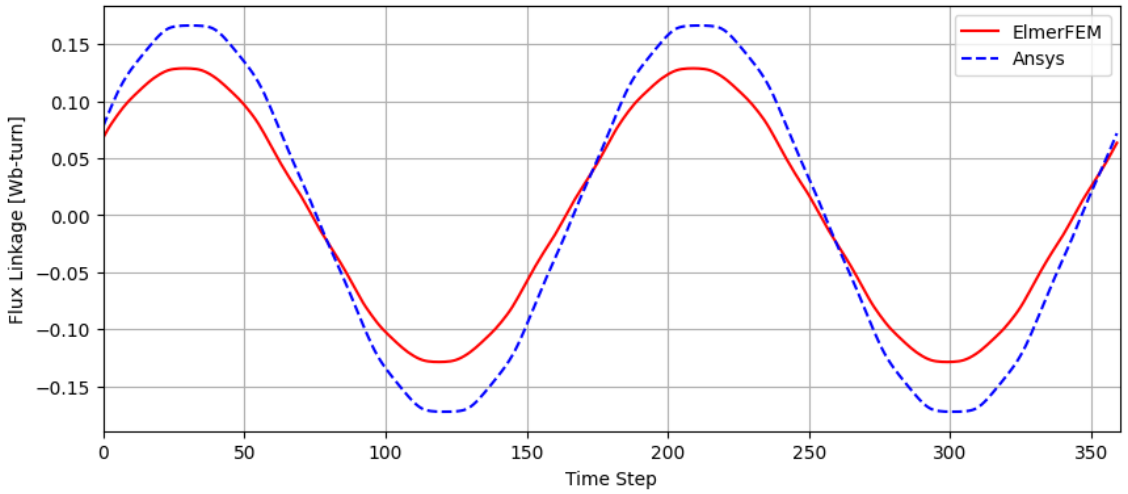


(a)

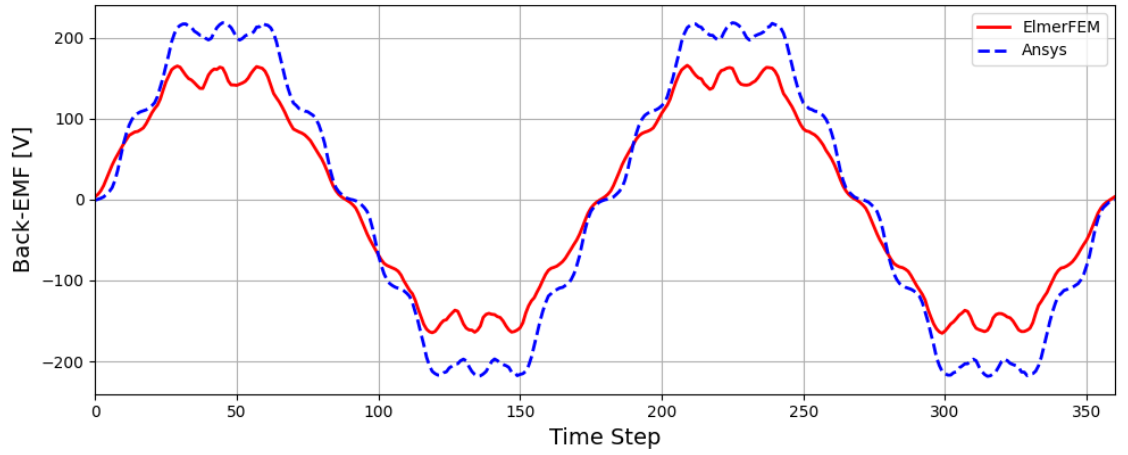


(b)

**Figure 5.3:** (a) Flux linkage. (b) Back-EMF.

Figure 5.3 shows the comparison of back-EMF computed from both tools respectively, for the same 2D model.

A discrepancy in amplitude can be observed between these two simulations. Specifically, the back-EMF predicted by ANSYS is approximately 50 V higher than that obtained from ElmerFEM. Similarly, a difference is also observed in flux linkage results, where the amplitudes are about 0.17 Wb for ANSYS and 0.13 Wb for ElmerFEM. Despite the amplitude deviation, the overall electromagnetic behavior is highly consistent. Both exhibit nearly identical local waveform characteristics, including the shapes of the peak regions, as well as the number and distribution of the small waveform kinks appearing along the rising and falling edges.

The difference in magnitude between the two tools may be caused by differences in mesh details and CAD geometry definitions. However, the consistency indicates that the two FEM environments can capture highly comparable characteristics, meaning that the adopted FEM setup is robust and reliable for 3D modeling.

### 5.1.4 2D multi-slice approximation of rotor skewing

As a 3D geometric feature, skewing cannot be directly represented in 2D FEM. To conduct an initial investigation of the effect of rotor skewing with minimum computational effort, the conventional multi-slice approximation can be initially employed in the 2D case without designing a completely skewed three-dimensional model, and computation time is much faster.

#### 5.1.4.1 Torque behavior

With the purpose of investigating the skewing effects on torque ripple and cogging torque, three rotor configurations presented in Figure 5.4 are simulated to observe the torque behavior, including the unskewed rotor, the linear step-skew rotor, and the V-shape skew rotor, which is also known as the herringbone rotor.

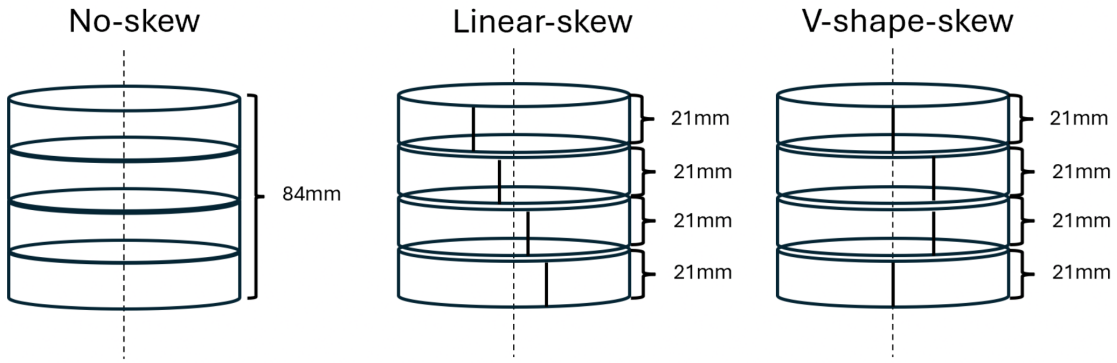


**Figure 5.4:** Skew configuration

The computation of cogging torque is carried out in a transient solver without current excitation, while the rotational speed is set at 3000 rpm. Torque behavior is shown in Figure 5.5

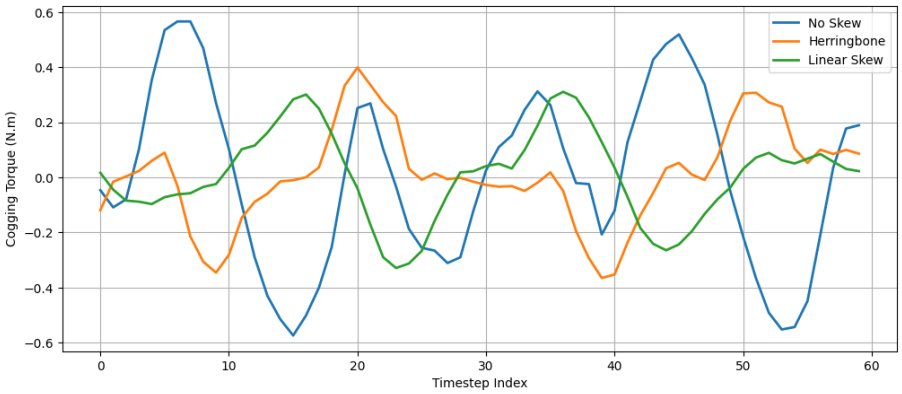


**Figure 5.5:** Cogging torque comparison

Similarly, the computation of torque ripple is conducted in the transient solver at the same condition but with current excitation; waveforms are illustrated in Figure 5.6.

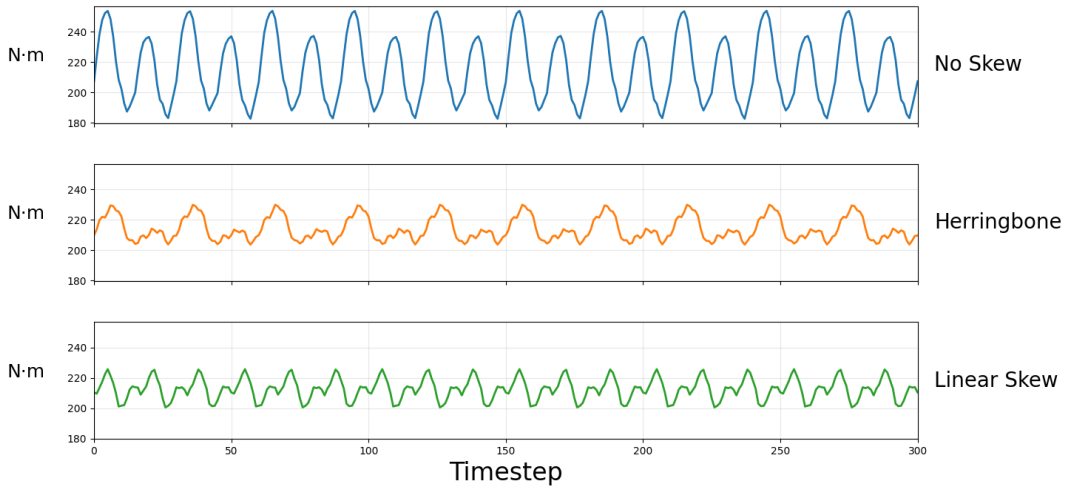


**Figure 5.6:** Torque ripple comparison

It can be clearly observed that the presence of rotor skew significantly affects the torque behavior. Compared with the unskewed motor, the skewed motor exhibits a noticeable suppression of torque fluctuations, resulting in a smoother torque waveform.

To further investigate the impact of different skew strategies, two quantitative metrics are introduced, namely the Normalized Torque Fluctuation (NTF) and the cogging torque peak-to-peak value. NTF is defined as

$$\mathrm{NTF} = \frac{T_{\max} - T_{\min}}{T_{\mathrm{avg}}} \tag{5.1}$$

where $T_{\max}$ and $T_{\min}$ represent the averaged maximum and minimum torque values, respectively, and $T_{\mathrm{avg}}$ represents the average torque.

In addition, the value of P2P reflecting the absolute variation of the cogging torque is given by

$$T_{\mathrm{cog,P2P}} = T_{\max} - T_{\min} \tag{5.2}$$

The quantified results for the investigated configurations are summarized in Table 5.1.

**Table 5.1:** Skewing vs torque ripple and cogging torque

| Skewing Type | Segment | Skew Angle | NTF | Cogging P2P | Avg. Torque |
|---|---|---|---|---|---|
| No-skew | 1 | 0° | 30.6 % | 1.1 N·m | 214.3 N·m |
| Linear skew | 4 | 2.5° | 11.9 % | 0.6 N·m | 212 N·m |
| Herring | 4 | 3.75° | 12.2 % | 0.8 N·m | 213.9 N·m |

It is evident from the table that the introduction of skew significantly reduces both NTF and the cogging torque. The unskewed case exhibits a relatively high fluctuation level, whereas all skewed configurations achieve substantial improvements. Among the investigated strategies, the 4-segment linear step skew rotor yields the lowest normalized torque fluctuation. NTF is reduced significantly from 30.6 % to approximately 11.9 % compared to the baseline. In terms of cogging torque, the same configuration also achieves a relatively low peak-to-peak value, with the cogging torque decreasing from 1.1 N·m to around 0.6 N·m, indicating the best overall performance.

#### 5.1.4.2 Core loss

As one of the most important indicators of the performance of a motor, losses also need to be evaluated under different skewing configurations. In this thesis, the same three models considered in the previous torque study are used to assess the core loss characteristics.

The simulated core loss results for the three skewing configurations are presented in Figure 5.7. These results provide a direct comparison of the influence of different skewing strategies on the core loss characteristics of the motor.

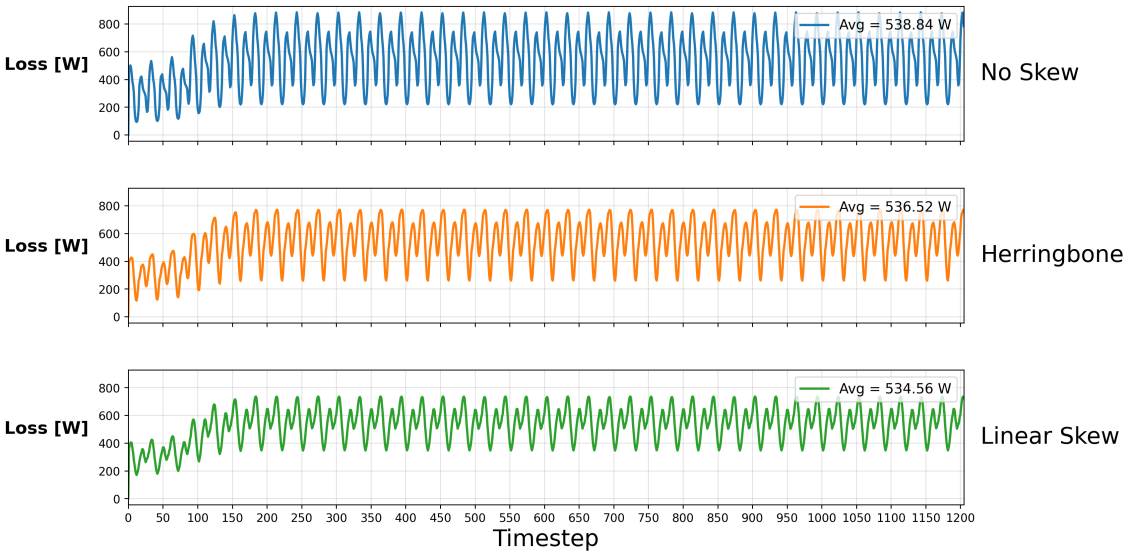


**Figure 5.7:** Core loss comparison

Since mechanical losses, windage losses, and other parasitic losses are not included in the present simulation, a simplified normalized loss indicator is adopted for comparative purposes and expressed as

$$\eta^* = \frac{P_{\text{core}}}{T_{\text{avg}}\omega} \times 100\ \% \tag{5.3}$$

where $P_{\text{core}}$ denotes the average core loss, $T_{\text{avg}}$ is the average electromagnetic torque, and $\omega$ represents the mechanical angular velocity. The term $T_{\text{avg}}\omega$ corresponds to the mechanical output power of the machine. This metric is used to evaluate the relative contribution of core loss to the output power for different skew topologies.

**Table 5.2:** Comparison of normalized core-loss indicator for different skew topologies

| **Skewing Type** | $P_{\text{core}}$ **(W)** | $\eta^*$ **(%)** |
|---|---|---|
| No-skew | 538.84 | 0.801 |
| Linear skew | 534.56 | 0.804 |
| V-shape | 536.52 | 0.798 |

The quantitative comparison of the average core loss and the normalized loss indicator for different skew topologies is summarized in Table 5.2.

The loss waveforms indicate that the influence of different skew topologies on the fluctuation characteristics of the core loss. The no-skew configuration exhibits the strongest transient fluctuation. The herringbone-skew topology effectively reduces the loss fluctuation, while the linear-skew topology presents the smoothest loss waveform with the minimum oscillation amplitude.

In terms of average core loss, the differences among the three configurations are negligible. The average core losses of the no-skew, herringbone-skew, and linear-skew models are 538.84 W, 536.52 W, and 534.56 W, respectively. The corresponding normalized loss indicators $\eta^*$ are all approximately 0.8 %, with only negligible differences among the three configurations.

## 5.2 3D Electromagnetic characteristics

A full 3D model is established to further investigate the detailed electromagnetic field distribution inside the motor under more realistic conditions. Based on the full 3D model, key electromagnetic quantities, including flux linkage and back-EMF, are evaluated and compared with the corresponding results obtained from the 2D model.

Additionally, the 3D model is mainly used to analyze the harmonic components of the back-EMF and the corresponding THD, providing further insight through comparison with the multi-slice method.

### 5.2.1 3D electromagnetic field analysis

Visualization provides a more intuitive way to study the electromagnetic properties of a 3D FEM model. Figure 5.8 shows the magnetic vector potential magnitude and magnetic flux density distribution of the unskewed 3D motor, respectively.

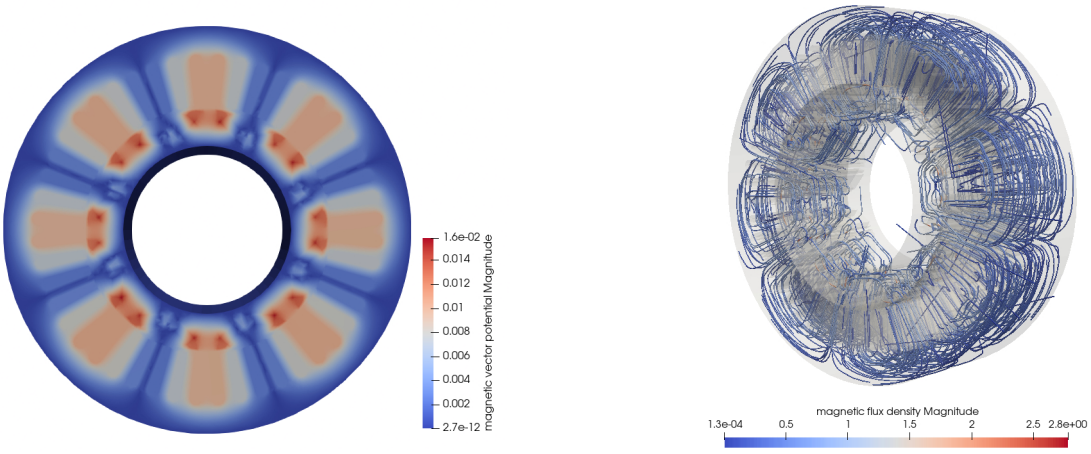


(a) (b)

**Figure 5.8:** Distribution of Magnetic Vector Potential and Magnetic Flux Density

The distributions of magnetic vector potential $A$ and magnetic flux density $B$ showed good spatial agreement with the pole configuration of the machine. The regions with high magnetic vector potential variation corresponded well to the regions with strong magnetic flux density, especially around the permanent magnets and rotor bridges. This relationship is consistent with Equation (3.12) which indicates that the magnetic flux density is derived from the curl of the magnetic vector potential. The highest flux density was observed around the rotor bridge region, where the magnetic flux became highly concentrated and approached approximately 2 T, which indicates the local magnetic saturation. The flux-line distribution also followed the expected pole-number arrangement, confirming that the developed 3D model was able to accurately capture the main magnetic field characteristics and flux paths inside the machine.

## 5.3 Electromagnetic Comparison Between 2D and 3D Models

To begin with, the consistency between the 2D and 3D FEM models was evaluated through comparisons of flux linkage, back-EMF, and harmonic characteristics.

Figure 5.9 shows the flux linkage and back-EMF of both the 2D and 3D Prius PMSM models without skew. It is noted that the waveform behavior of the three-phase flux linkage and back-EMF for the 3D model is highly consistent with those of the 2D model, meaning that the fully extruded 3D model is able to preserve the primary electromagnetic properties of the machine.

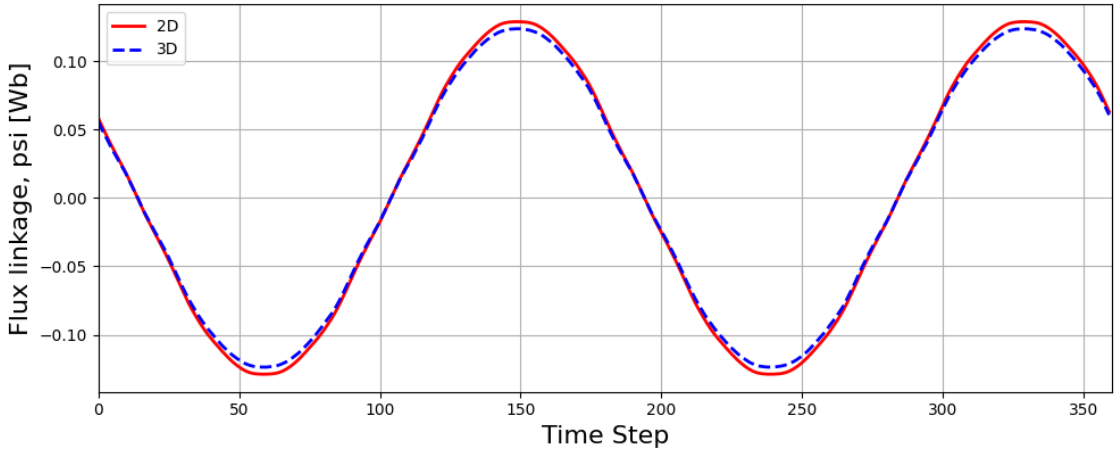


(a)

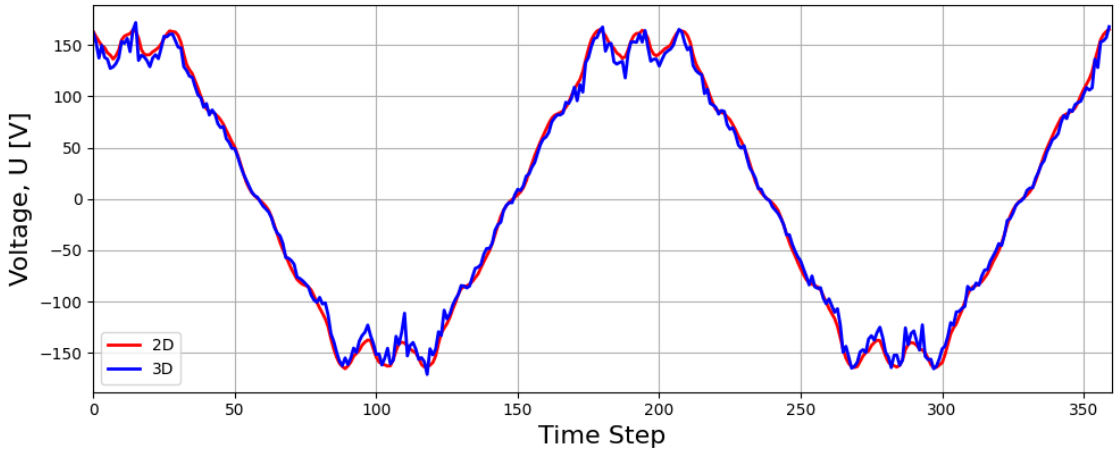


(b)

**Figure 5.9:** (a) Flux linkage 3D vs 2D. (b) Back-EMF 3D vs 2D

The reduction in the amplitude of the three-phase flux linkage and back-EMF can be seen in the 3D model. The maximum value of the three-phase flux linkage drops slightly from 130 mWb in the 2D model to about 128 mWb in the 3D model, and the fundamental component amplitude drops from 162 V in the 2D model to about 156 V in the 3D model as shown in Figure 5.10. However, in spite of this amplitude drop, the stability and continuity of the waves are preserved without any numerical anomalies.

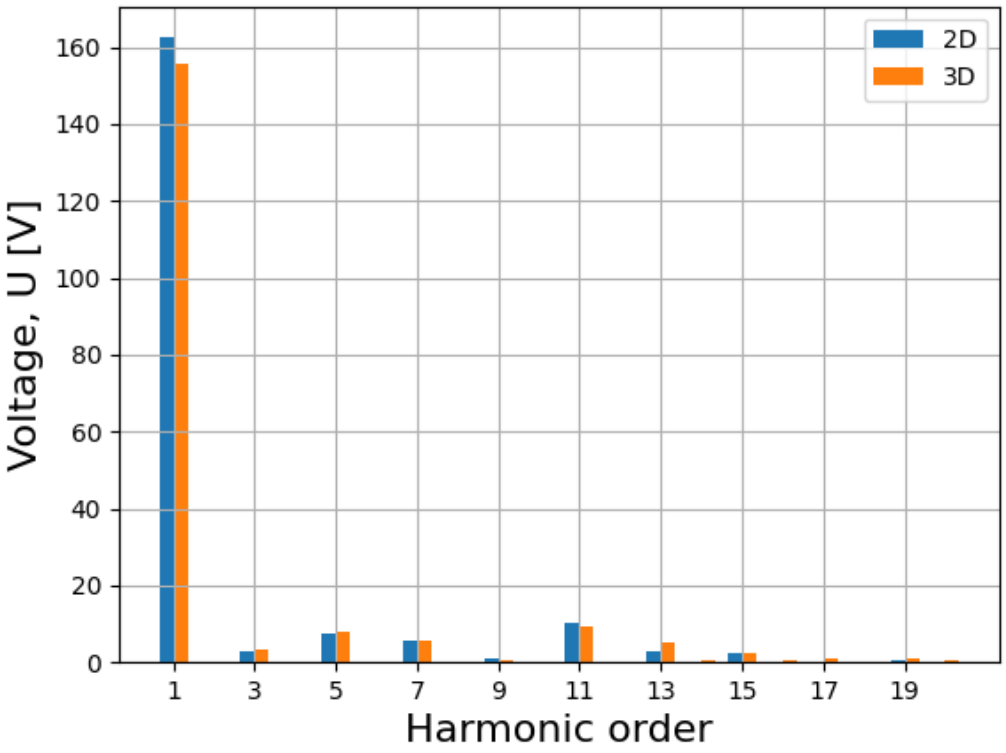


**Figure 5.10:** Comparison of harmonic content of back-EMF

This shows that the established 3D FEM model is able to reflect the primary electromagnetic properties of the machine and, additionally, the electromagnetic field characteristics of the 3D model.

### 5.3.1 Skewing impact on harmonic

The harmonic content of back-EMF is closely related to torque ripple since the interaction between the harmonic magnetic field and stator currents generates additional pulsating torque components.

A corresponding multi-slice approximation is carried out for the two-segment skewed rotor configurations to provide a reference for the subsequent full 3D harmonic comparison.

Figure 5.11 shows the harmonic comparison obtained from the simplified multi-slice skew approximation and full 3D, respectively. It can be observed in plot (a) that the fundamental harmonic component remains relatively stable for different skew angles, while several higher-order harmonic components, especially the $11^{\text{th}}$ and $13^{\text{th}}$ are reduced after skewing is introduced.

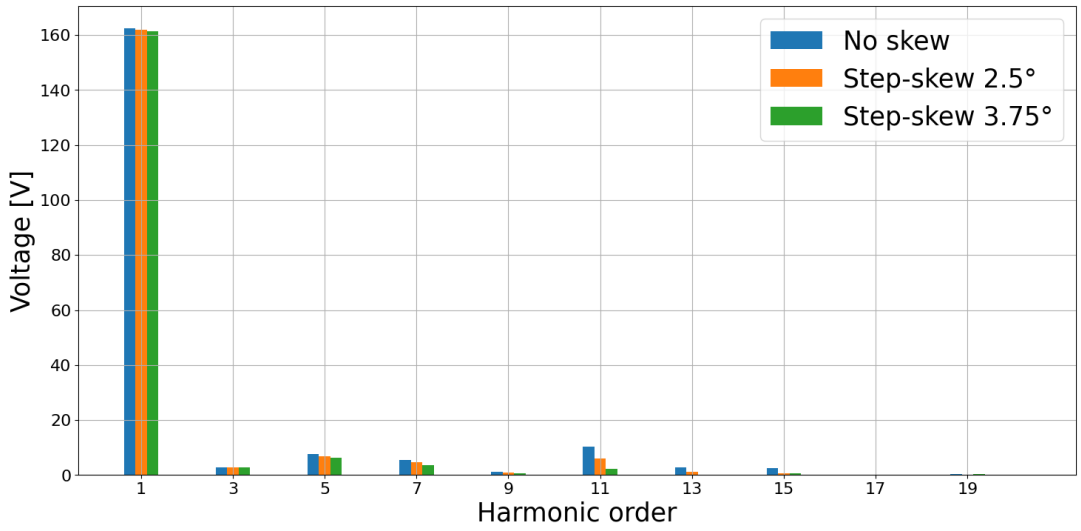


(a)

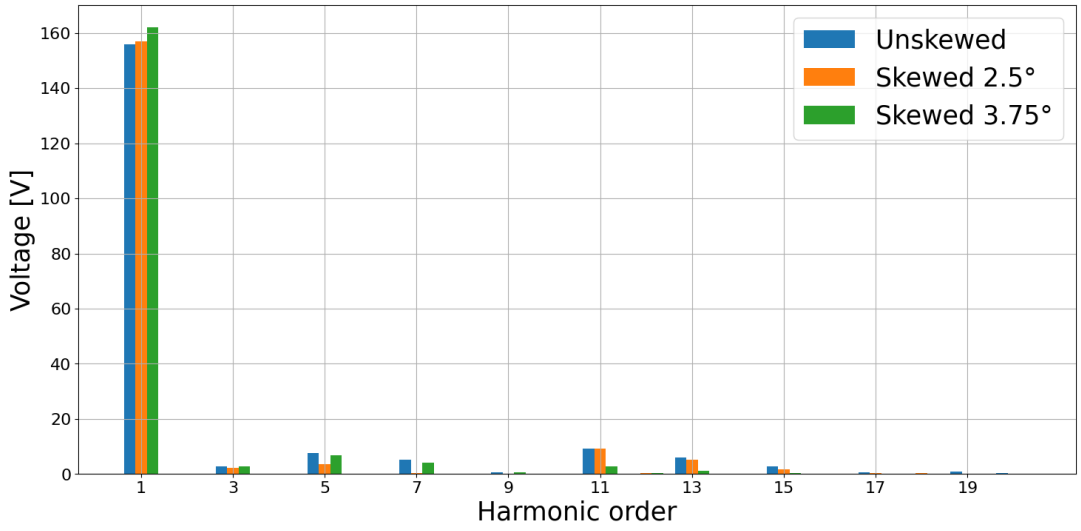


(b)

**Figure 5.11:** (a) Multi-slice harmonic (b) 3D harmonic

Plot(b) is the back-EMF harmonic obtained from the full 3D model. It can be observed that he overall harmonic distribution trend remains similar. In this section, the influence of different skew angles on the harmonic characteristics of the 3D PMSM model is further investigated.

It can be observed that the magnitude of the fundamental harmonic component remains relatively similar at around 160 V for different skew angles, indicating that rotor skewing does not significantly affect the primary operating characteristics of the machine. At the same time, several higher-order harmonic components decrease as the skew angle approaches half the slot angle. In particular, the $11^{\text{th}}$ and $13^{\text{th}}$ harmonics drop significantly to nearly 0 in the 3.75° skewed model.

To quantify the distortion of the back-EMF waveform, the THD is evaluated for different skew angles, and the results are summarized in Table 5.3. For both the multi-slice and 3D models, the skewed cases exhibit lower THD values compared with the corresponding unskewed cases. In particular, the 2.5° skewed model already shows a noticeable reduction in THD, decreasing from 9.16 % to 6.62 % in the multi-slice model, and from 9.69 % to 7.39 % in the 3D model. Among the investigated configurations, the 3.75° skewed model gives the lowest THD, with values of 5.04 % for the multi-slice model and 5.59 % for the 3D model. These results provide a quantitative comparison of the effect of different skew angles on the harmonic distortion of the back-EMF.

**Table 5.3:** Total Harmonic Distortion (THD)

| **Case** | **Skew Angle (°)** | **THD (%)** |
|---|---|---|
| Unskewed motor(2D) | 0.0 | 9.16 |
| Skewed motor(2D) | 2.5 | 6.62 |
| Skewed motor(2D) | 3.75 | 5.04 |
| Unskewed motor(3D) | 0.0 | 9.69 |
| Skewed motor(3D) | 2.5 | 7.39 |
| Skewed motor(3D) | 3.75 | 5.59 |

Among the investigated cases, the 3.75° skewed model gives the lowest THD. This skew angle introduces a special phase shift between different axial sections, causing the high-order harmonics, especially the $11^{\text{th}}$ and $13^{\text{th}}$ components become close to opposite phase and cancel each other in the total back-EMF. As a result, the harmonic distortion is significantly reduced, which contributes to the suppression of torque ripple.

# 6
# Conclusion

Skewing configurations reduced the fluctuation of cogging torque and torque ripple while having a limited impact on electromagnetic performance; 4-segment linear skew introduced in the original model showed better performance, reducing cogging torque from 1.1 N.m to 0.6 N.m and torque ripple from 30.6 % to 11.9 %. At the same time, the average torque remained nearly unchanged at about 213 N·m for different skewing configurations, while the core loss stayed close to 536 W, and the normalized core loss indicator remained around 0.8 %.

The full 3D model preserved the main electromagnetic characteristics of the 2D model under more realistic conditions. The comparison between the 2D and 3D models showed good agreement in flux linkage, back-EMF, and harmonic behavior. The maximum flux linkage changed from about 130 mWb in the 2D model to about 128 mWb in the 3D model, while the fundamental component of back-EMF changed from about 162 V to about 156 V.

Regarding back-EMF harmonics, the $11^{\text{th}}$ and $13^{\text{th}}$ order dropped to almost 0 in the 3.75° skew angle design, while the fundamental component remained almost unchanged at about 160 V; in terms of THD of the back-EMF, it was reduced from 9.69% in the unskewed 3D model to 5.59 % .This effect is caused by a phase shift along the axial direction of the motor; some slot-related harmonic components are canceled out between two sections of the rotor. Based on the simulation results, a skew angle corresponding to half of the slot pitch improves the back-EMF characteristics while reducing the THD.

Full 3D simulations require much higher computational resources than 2D. The 2D transient simulation took about 8600 seconds, whereas the full 3D simulation required about 60000 seconds even with 256-processor parallel computation. Therefore, the multi-slice method is useful for fast analysis, while the full 3D model provides more detailed electromagnetic information.

# 7

# Proposed continuation items

Based on the present 2D and 3D framework developed in this thesis work, several directions remain available for further extension and improvement

## 7.1 Improvement of Simulation Accuracy

The first step of the future work is to further improve the electromagnetic simulations through refined mesh quality, optimized boundary condition settings and fine-tuned iteration parameters.

## 7.2 Electromagnetic-Structural Coupling

By introducing material properties such as Young's modulus, Poisson's ratio, and density in material definition, electromagnetic-structural coupled simulations could be run to investigate the structural response and vibration behavior of the skewed PMSMs under different operating conditions. Such studies can provide further insight into the interaction between spatial electromagnetic fields and mechanical deformation in electrical machines.

## 7.3 Automation for Optimization

As part of future work, automation based on Dakota [47] will be further developed to explore a wider design space. In particular, more skew configurations, such as different skew angles, segment numbers, and topologies, can be included to extend the current study and perform better comparisons. In addition, several performance indicators, such as the back-EMF THD, torque ripple, and efficiency, can be considered together to better understand the trade-offs between different designs.

# Bibliography


[1] Gustaver, M. (2020) A Chalmers University of Technology Master's thesis template for LaTeX. Unpublished.

[2] Volvo Cars, *EX60 Electric*, Gothenburg, Sweden: Volvo Car Corporation, 2026.

[3] P. Pillay and R. Krishnan, "Modeling, simulation, and analysis of permanent-magnet motor drives. I. The permanent-magnet synchronous motor drive," *IEEE Transactions on Industry Applications*, vol. 25, no. 2, pp. 265–273, 1989. Available at: `https://ieeexplore.ieee.org/stamp/stamp.jsp?tp=&arnumber=25541`

[4] Z. Q. Zhu and D. Howe, "Influence of Design Parameters on Cogging Torque in Permanent Magnet Machines," *IEEE Transactions on Energy Conversion*, vol. 15, no. 4, pp. 407–412, 2000. Available at: `https://ieeexplore.ieee.org/stamp/stamp.jsp?tp=&arnumber=4168032`

[5] A. E. Fitzgerald, C. Kingsley, Jr., and S. D. Umans, *Electric Machinery*, 5th ed., New York, NY, USA: McGraw–Hill, 2003.

[6] J. R. Hendershot and T. J. E. Miller, *Design of Brushless Permanent-Magnet Motors*, New York, NY, USA: McGraw–Hill, 1994.

[7] P. Ponomarev *et al.*, "Finite Element Analysis of Permanent Magnet Synchronous Machines Using ElmerFEM," CSC – IT Center for Science, Electromagnetics Tutorial.

[8] S. Naik, B. Bag, and K. Chandrasekaran, "A 2D and 3D Analysis on Electromagnetic Parameters of Spoke-Shape Interior Permanent Magnet Synchronous Motor Using FEM," *Periodica Polytechnica Electrical Engineering and Computer Science*, vol. 67, no. 2, pp. 181–193, 2023. Available at: `https://pp.bme.hu/eecs/article/view/20835`

[9] M. Pechlivanidou *et al.*, "Comparative Study on 2D and 3D Magnetic Field Analysis of Permanent Magnet Synchronous Motor Using FEM," *Journal of Electromagnetic Waves and Applications*, 2013.

[10] X. Xiaodong *et al.*, "Influence of Skew Angle on Electromagnetic Performance of Permanent Magnet Synchronous Motors," *IEEE Transactions on Industry Applications*, 2018. Available at: `https://ieeexplore.ieee.org/stamp/stamp.jsp?tp=&arnumber=8540892`

[11] H. Sasaki and H. Igarashi, "Topology Optimization Accelerated by Deep Learning," *IEEE Transactions on Magnetics*, vol. 55, no. 6, 2019. Available at: `https://ousar.lib.okayama-u.ac.jp/files/public/6/67879/20241218174841610123/fulltext.pdf`,

[12] ANSYS Inc., *ANSYS Maxwell 2D Field Simulator v14 User's Guide: Study of a Permanent Magnet Motor with MAXWELL 2D—Example of the 2004 Prius IPM Motor*, ANSYS Documentation.

[13] M. S. Rafaq, W. Midgley, and T. Steffen, "A Review of the State of the Art of Torque Ripple Minimization Techniques for Permanent Magnet Synchronous Motors," *IEEE Transactions on Industrial Informatics*, vol. 20, no. 1, pp. 1019–1031, 2024, doi: 10.1109/TII.2023.3272689. Available at: `https://ieeexplore.ieee.org/document/8673771`,

[14] Wikipedia contributors, "Maxwell's equations," *Wikipedia, The Free Encyclopedia*. Available: `https://en.wikipedia.org/wiki/Maxwell`

[15] Wikipedia contributors, *Gauss's law*, Wikipedia, The Free Encyclopedia. Available: `https://en.wikipedia.org/wiki/Gauss%27s_law`

[16] Wikipedia contributors, *Gauss's law for magnetism*, Wikipedia, The Free Encyclopedia. Available: `https://en.wikipedia.org/wiki/Gauss%27s_law_for_magnetism`

[17] Wikipedia contributors, *Faraday's law of induction*, Wikipedia, The Free Encyclopedia. Available: `https://en.wikipedia.org/wiki/Faraday%27s_law_of_induction`

[18] Physics @ Georgia Tech, *Ampere-Maxwell Law*. Available: `https://www.physicsbook.gatech.edu/Ampere-Maxwell_Law`

[19] Wikipedia contributors, *Mathematics of three-phase electric power*, Wikipedia, The Free Encyclopedia. Available: `https://en.wikipedia.org/wiki/Mathematics_of_three-phase_electric_power`

[20] Wikipedia contributors, "Clarke transformation," *Wikipedia, The Free Encyclopedia*. Available: `https://en.wikipedia.org/wiki/Alpha%E2%80%93beta_transformation`

[21] Wikipedia contributors, "Park transformation," *Wikipedia, The Free Encyclopedia*. Available: `https://en.wikipedia.org/wiki/Direct-quadrature-zero_transformation`

[22] *Universal Inverters for e-Motor Development and Testing*, Apr. 19, 2024. [Online]. Available at: `https://www.unico.com/universal-inverters-for-e-motor-development-testing/`

[23] Wikipedia contributors, *Flux linkage*, Wikipedia, The Free Encyclopedia. Available: `https://en.wikipedia.org/wiki/Flux_linkage`

[24] Wikipedia contributors, *Stokes' theorem*, Wikipedia, The Free Encyclopedia. Available: `https://en.wikipedia.org/wiki/Stokes%27_theorem`

[25] Wikipedia contributors, *Lenz's law*, Wikipedia, The Free Encyclopedia. Available: `https://en.wikipedia.org/wiki/Lenz%27s_law`

[26] Wikipedia contributors, "Fourier series," *Wikipedia*. [Online]. Available: `https://en.wikipedia.org/wiki/Fourier_series`. Accessed: Apr. 15, 2026.

[27] Wikipedia contributors, *Total harmonic distortion*, Wikipedia, The Free Encyclopedia. Available: `https://en.wikipedia.org/wiki/Total_harmonic_distortion`

[28] Wikipedia contributors, *Cogging torque*, Wikipedia, The Free Encyclopedia. Available: `https://en.wikipedia.org/wiki/Cogging_torque`

[29] MathWorks, *PMSM Torque Estimator*, Available: https://www.mathworks.com/help/sps/ref/pmsmtorqueestimator.html

[30] *Power Losses Models for Magnetic Cores: A Review*, Daniela Rodriguez-Sotelo, Martin A. Rodriguez-Licea, Ismael Araujo-Vargas, Juan Prado-Olivarez, Alejandro-Israel Barranco-Gutiérrez and Francisco J. Perez-Pinal, *Micromachines*, vol. 13, no. 3, Art. 418, March 2022. Available at: https://www.mdpi.com/2072-666X/13/3/418

[31] *Eddy Current*, Wikipedia, The Free Encyclopedia. Available at: https://en.wikipedia.org/wiki/Eddy_current#Power_loss

[32] *Elmer, an open source multiphysical simulation software*, Available at: https://research.csc.fi/service/elmer/,

[33] Wikipedia contributors, *Residual (numerical analysis)*, Wikipedia, The Free Encyclopedia. Available: https://en.wikipedia.org/wiki/Residual_(numerical_analysis)

[34] *ElmerSolver Manual*, Juha Ruokolainen, Mika Malinen, Peter Råback, Thomas Zwinger, Antti Pursula and Mikko Byckling,CSC – IT Center for Science, January 20, 2026. Available at: https://www.nic.funet.fi/index/elmer/doc/ElmerSolverManual.pdf

[35] Wikipedia contributors, "Krylov subspace," *Wikipedia, The Free Encyclopedia*. Available at: https://en.wikipedia.org/wiki/Krylov_subspace

[36] *Gmsh: A Three-Dimensional Finite Element Mesh Generator with Built-in Pre- and Post-Processing Facilities*, Christophe Geuzaine and Jean-François Remacle, International Journal for Numerical Methods in Engineering, Vol. 79, No. 11, pp. 1309–1331, 2009. Available at: https://gmsh.info/doc/preprints/gmsh_paper_preprint.pdf

[37] *ParaView: An End-User Tool for Large Data Visualization*, Available at: https://www.paraview.org/

[38] *ThinLinc, a Linux remote desktop server*, Cendio AB, 2026. Available at: https://www.cendio.com/thinlinc/

[39] *COMSOL Multiphysics Material Library*, COMSOL, Inc. Available at: https://www.comsol.com/

[40] F. Cardarelli, *Materials Handbook: A Concise Desktop Reference*, Springer, 2008.

[41] *Engineering Toolbox: Material Properties*, Available at: https://www.engineeringtoolbox.com

[42] P. Råback, M. Malinen, J. Ruokolainen, A. Pursula, T. Zwinger (Eds.), *Elmer Models Manual*, CSC – IT Center for Science, January 20, 2026.

[43] Wikipedia, *Steinmetz's equation*, Available at: https://en.wikipedia.org/wiki/Steinmetz%27s_equation

[44] Wikipedia, *Galerkin method*, Available at: https://en.wikipedia.org/wiki/Galerkin_method

[45] P. Ponomarev, *Elmer FEM: Induction Machine Tutorial*, VTT Technical Research Centre of Finland, Research Report VTT-R-02819-17, 2017.

[46] ANSYS, Inc., *Ansys Maxwell | Electromechanical Device Analysis Software*, Available: https://www.ansys.com/products/electronics/ansys-maxwell

[47] Dakota Automation, Inc., *Dakota Automation – Factory Automation and Automated Equipment*, Available: `https://dakotaautomation.com/`, accessed: May 14, 2026.

**DEPARTMENT OF SOME SUBJECT OR TECHNOLOGY**
**CHALMERS UNIVERSITY OF TECHNOLOGY**
Gothenburg, Sweden
www.chalmers.se


CHALMERS
UNIVERSITY OF TECHNOLOGY